Hydrophobic Polyamide Nanofilms Provide Rapid Transport for Crude Oil Separation

Siyao Li[1], Ruijiao Dong[1,2], Valentina-Elena Musteata[3], Jihoon Kim[1,4,7], Neel D. Rangnekar[5], J. R. Johnson[5], Bennett D. Marshall[5], Stefan Chisca[3], Jia Xu[1,6], Scott Hoy[5], Benjamin A. McCool[5], Suzana P. Nunes[3], Zhiwei Jiang[1,7]*, Andrew G. Livingston[1,7]*

Affiliations:

[1]Barrer Center, Department of Chemical Engineering, Imperial College London, South Kensington Campus, London SW7 2AZ, UK.

[2]Shanghai Center for Systems Biomedicine, Key Laboratory of Systems Biomedicine, Shanghai Jiao Tong University, Shanghai 200240, China.

[3]King Abdullah University of Science and Technology, Biological and Environmental Science and Engineering Division, Advanced Membranes and Porous Materials Center, Thuwal, Saudi Arabia.

[4]Process Design and Research Center, Chemical and Process Technology Division, Korea Research Institute of Chemical Technology, Daejeon, 34114, South Korea.

[5]Corporate Strategic Research, ExxonMobil Research and Engineering, Annandale, NJ 08801, USA.

[6]Key Laboratory of Marine Chemistry Theory and Technology (Ministry of Education), School of Materials Science and Engineering, College of Chemistry and Chemical Engineering, Ocean University of China, Qingdao, 266100, China

[7]Department of Engineering and Materials Science, Queen Mary University of London, Mile End Road, London E1 4NS, UK.

*Corresponding author. Email: zhiwei.jiang@qmul.ac.uk; a.livingston@qmul.ac.uk

Abstract: Hydrocarbon separation relies on energy-intensive distillation. Membrane technology can offer an energy-efficient alternative, but requires selective differentiation of crude oil molecules with rapid liquid transport. We synthesized multiblock oligomer amines, comprising a central amine segment with two hydrophobic oligomer blocks, and used them to fabricate hydrophobic polyamide nanofilms by interfacial polymerization from self-assembled vesicles. These polyamide nanofilms provide >100 times faster transport of hydrophobic liquids than conventional hydrophilic counterparts. In the fractionation of light crude oil, manipulation of the film thickness down to ~10 nanometers achieves one order of magnitude higher permeance than current state-of-the-art hydrophobic membranes, while retaining comparable size- and class-based separation. This high permeance can significantly reduce plant footprint, expanding the potential for utilizing membranes comprising ultrathin nanofilms in crude oil fractionation.

Separation and purification play a crucial role in the oil and gas industry, but rely upon energy-intensive distillation processes, which account for 10-15% of global energy use (*1*). Membrane-based separation has emerged as a promising alternative due to its innate advantage of low energy consumption. One successful example is the production of fresh water from seawater by reverse osmosis (*2*). Thin film composite membranes manufactured via interfacial polymerization show exceptional water permeance and high salt rejection, achieved through their thin and highly crosslinked polyamide selective layer (*2*). Seeking a similar paradigm change, organic solvent reverse osmosis has been developed for molecular separations in organic liquids (*3, 4*), and applied to the fractionation of crude oil (*5, 6*).

However, thin film composite membranes made from conventional chemistry exhibit limited permeance of hydrocarbon liquids, due to the hydrophilic nature of polyamide or polyester networks in the separating layer (*7-9*). To enhance the hydrophobicity, attempts have been made to cap the polyamide layer with hydrophobic groups or introduce hydrophobic groups to the monomers used during the interfacial reaction (*10-15*). The permeance-selectivity range of the resulting membranes improved, but the permeance remains too low for industrial crude separation (*5, 6, 16*). Therefore, creating hydrophobic separating layers with high permeances for non-polar liquids and tight selectivities for crude oil fractions remains of interest.

We report the fabrication of ultrathin hydrophobic polyamide nanofilms from vesicles of self-assembled multiblock oligomer amines (MOAs) via interfacial polymerization, and their performance in hydrocarbon separations. Amphiphilic MOAs, including a fluorine oligomer series and an alkane oligomer series, were synthesized by functionalizing the two ends of a hydrophilic precursor, pentaethylenehexamine (N_6), with hydrophobic inert oligomers containing R-OH (R=I to VI) (Fig. 1A, fig. S1). The two-step reaction employed carbonyldiimidazole as a coupling agent,

through which we tuned the MOA structure by attaching oligomers of increasing length. Nuclear magnetic resonance and Fourier transform infrared spectroscopy confirmed the formation of MOAs, including $F_5N_6F_5$, $F_9N_6F_9$, $F_{13}N_6F_{13}$, $C_3N_6C_3$, $C_6N_6C_6$ and $C_{10}N_6C_{10}$ (figs. S2-S8).
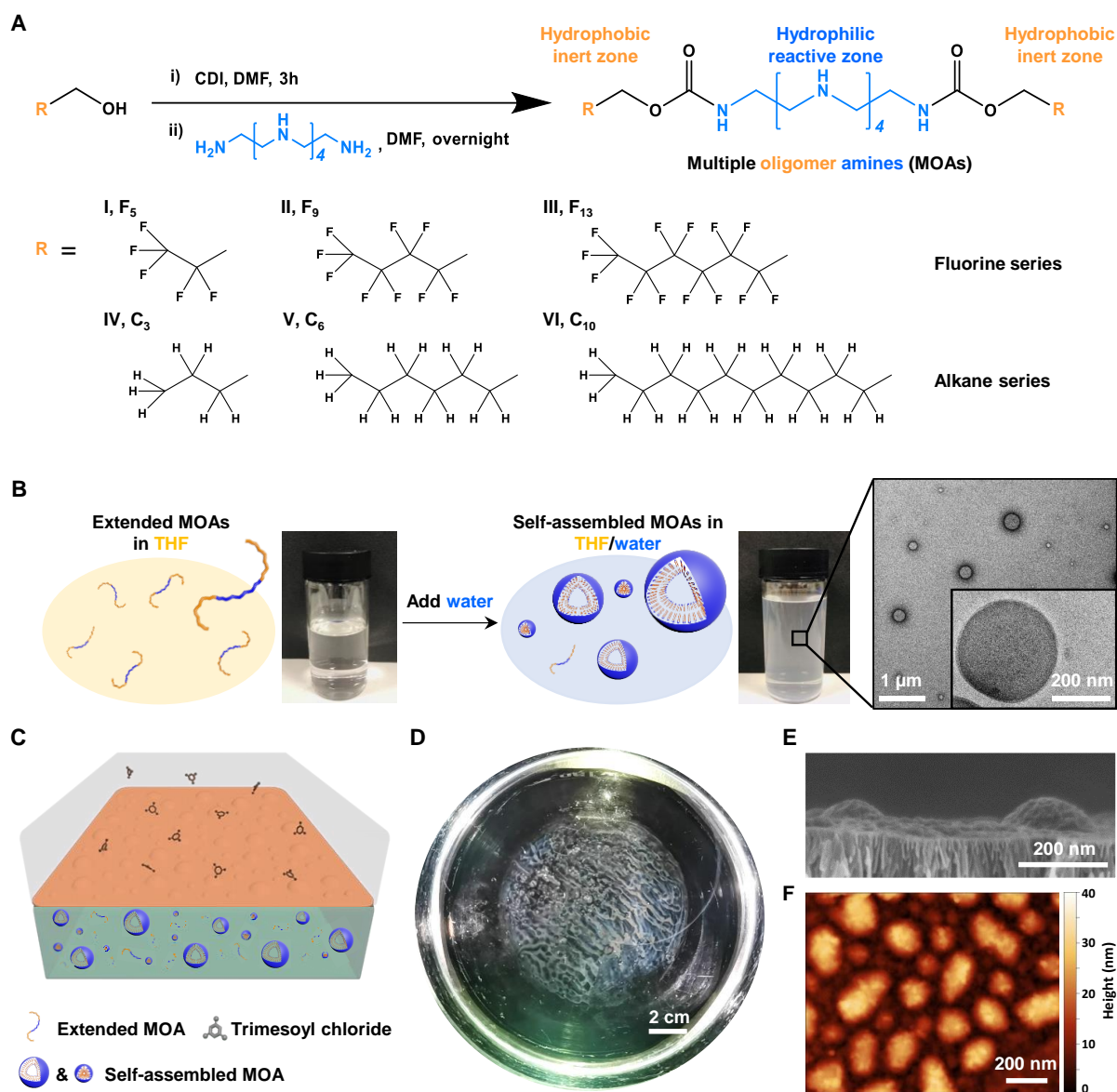
Fig. 1. Fabrication of hydrophobic polyamide nanofilms with multiblock oligomer amines (MOAs). (A) Synthetic route to MOAs with different oligomers R-OH (R=I to VI) using carbonyldiimidazole (CDI) as coupling agent. I=F_5, II=F_9, III=F_{13}, IV=C_3, V=C_6, and VI=C_{10}. **(B)**

Schematic and photographs of extended MOAs in tetrahydrofuran (THF), which formed self-assembled micelles or vesicles by addition of water. The inset shows a TEM image of $F_5N_6F_5$ (0.1 wt.%) self-assembled MOAs with core-shell structure. **(C)** Fabrication of ultrathin polyamide nanofilms by interfacial polymerization at a free interface between a hexane phase containing trimesoyl chloride and an aqueous phase (95 wt.% water and 5 wt.% THF) containing MOAs. **(D)** Photograph of a freestanding nanofilm transferred from the free interface onto a water-air surface. **(E)** Cross-sectional SEM image of the ultrathin nanofilm transferred onto an alumina support. **(F)** AFM height image of the ultrathin nanofilm transferred onto a silicon wafer. Both images reveal the incorporation of MOA vesicles into the nanofilms.

MOAs were readily soluble in tetrahydrofuran (THF), forming a clear solution (Fig. 1B). Upon addition of water to reach a 95/5 water/THF mixture, when present above the critical aggregation concentration (CAC), the MOAs self-assemble into nano-scale micelles or vesicles (Fig. 1B, figs. S9-S11), due to their inherent amphiphilicity (*17*). We conjecture that the spherical vesicles comprise aggregated hydrophobic oligomers facing inwards and extended hydrophilic amines facing outwards to the aqueous solution (*18*, fig. S12). Scanning electron microscope (SEM) and transmission electron microscope (TEM) images were consistent with the conjectured core-shell structure (Fig. 1B, fig. S13-S14).

Amines on the outer shell of MOA vesicles can react with trimesoyl chloride at a free aqueous-organic interface to fabricate a highly crosslinked polyamide nanofilm (Fig. 1C). The nanofilm comprises smooth surfaces formed from the extended MOAs with protuberances introduced by the vesicles present above the CAC. These nanofilms were flexible and robust, with no macroscopic defects observed while transferring them onto a water-air surface (Fig. 1D). When using more concentrated MOA solutions, nanofilms shrunk after transfer to the water surface (fig.

S15 and movie S1), consistent with their hydrophobicity. Free-standing nanofilms were then adhered onto porous polymeric supports and utilized as composite membranes (fig. S16). Both SEM cross-sectional images (Fig. 1E) and atomic force microscopy (AFM) images (Fig. 1F) reveal the existence of vesicles in the nanofilms, with ~200 nm diameters (figs. S17-S19), which matches well to the vesicle sizes measured in solution using dynamic light scattering (fig. S11).
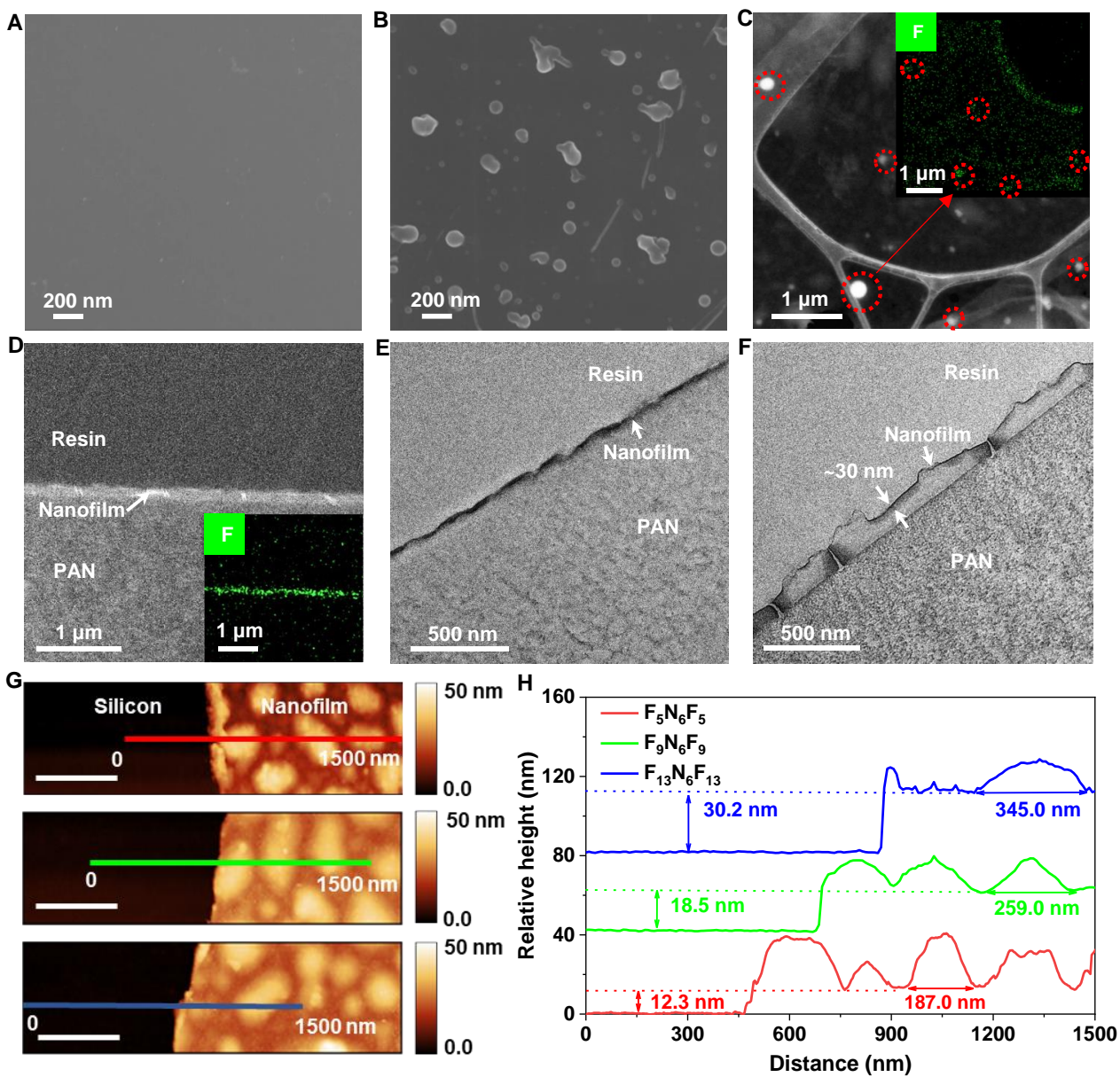
Fig. 2. Characterization of hydrophobic polyamide nanofilms fabricated from MOAs. SEM surface images of MOA nanofilms fabricated at **(A)** $F_5N_6F_5$ concentration (0.005 wt.%) below critical aggregation concentration (CAC), and **(B)** $F_5N_6F_5$ concentration (0.02 wt.%) above CAC. The protuberances correspond to vesicles of self-assembled MOAs. **(C)** TEM images of nanofilms made using 0.02 wt.% $F_9N_6F_9$ and corresponding fluorine mapping from EDX analysis (inset). **(D)** HAADF-STEM cross-sectional images of the nanofilm made using 0.1 wt.% $F_5N_6F_5$ and its EDX fluorine mapping (inset). TEM cross-sectional images of the nanofilm made from $C_6N_6C_6$ at **(E)** low concentration (0.005 wt.%) and **(F)** high concentration (0.1 wt.%), wherein the nanofilms were stained with ruthenium tetroxide to provide contrast for aromatic groups present in polyamide networks. The dense stripes in (F) reveal the active thickness of the nanofilm with hollow channels beneath. AFM height **(G)** image and **(H)** profiles of $F_5N_6F_5$ (0.02 wt.%), $F_9N_6F_9$ (0.02 wt.%), and $F_{13}N_6F_{13}$ (0.025 wt.%) nanofilms transferred onto silicon wafers for the measurement of nanofilm thickness. The profile lines across the protuberances provide width and height of MOA vesicles. The inset scale bar represents 400 nm.

We hypothesize that the vesicles provide enhanced hydrophobicity across the nanofilm due to the aggregation of hydrophobic segments in MOAs. To verify this hypothesis, smooth nanofilms without vesicles were produced by using a $F_5N_6F_5$ concentration below the CAC (Fig. 2A), exhibiting a water contact angle ~74° (fig. S20). This increased to ~93° for membranes incorporating vesicles using concentrations above the CAC (Fig. 2B, fig. S20), indicating high hydrophobicity (*19*), while retaining a similar crosslinking degree (fig. S21). TEM images and the corresponding element mapping demonstrate the fluorine distribution across the nanofilm (Figs. 2C and D). The dispersed fluorine content in the smooth regions corresponded to nanofilms formed by extended MOAs, in contrast to concentrated fluorine intensity in the vesicles (Fig. 2C), which

further enhanced with increasing MOA concentration (figs. S22 and S23). These results reveal the close proximity of fluorine oligomers inside the vesicles. The nanofilm was further stained with ruthenium tetroxide, which preferentially attaches to aromatic groups in the polyamide network (*20*). This enhances contrast and visibility of the polyamide separating layer under TEM (Figs. 2E and F). A smooth nanofilm was formed at concentrations below the CAC, whereas flattened vesicles were observed in nanofilms formed at MOA concentrations above the CAC. The high contrast across the vesicle surfaces reveals that the amines on the outer shell of vesicles reacted to form continuous crosslinked polyamide films during interfacial polymerization (Fig. 2F), which is chemically homogeneous to the smooth polyamide layer formed from extended MOAs. Further, interior of the vesicles shows no signs of staining, suggesting a hollow structure beneath the ~30 nm thick separating layer, despite the overall thickness of the vesicles being >100 nm. These vesicles were mechanically robust and conserved their structures after being pressurized at 10 bar (figs. S24 and S25). AFM images demonstrated that increasing the length of fluorine chains from $F_5N_6F_5$ to $F_{13}N_6F_{13}$ in MOA monomers led to a corresponding increase in the nanofilm thickness (Figs. 2G and H, figs. S26-S28).
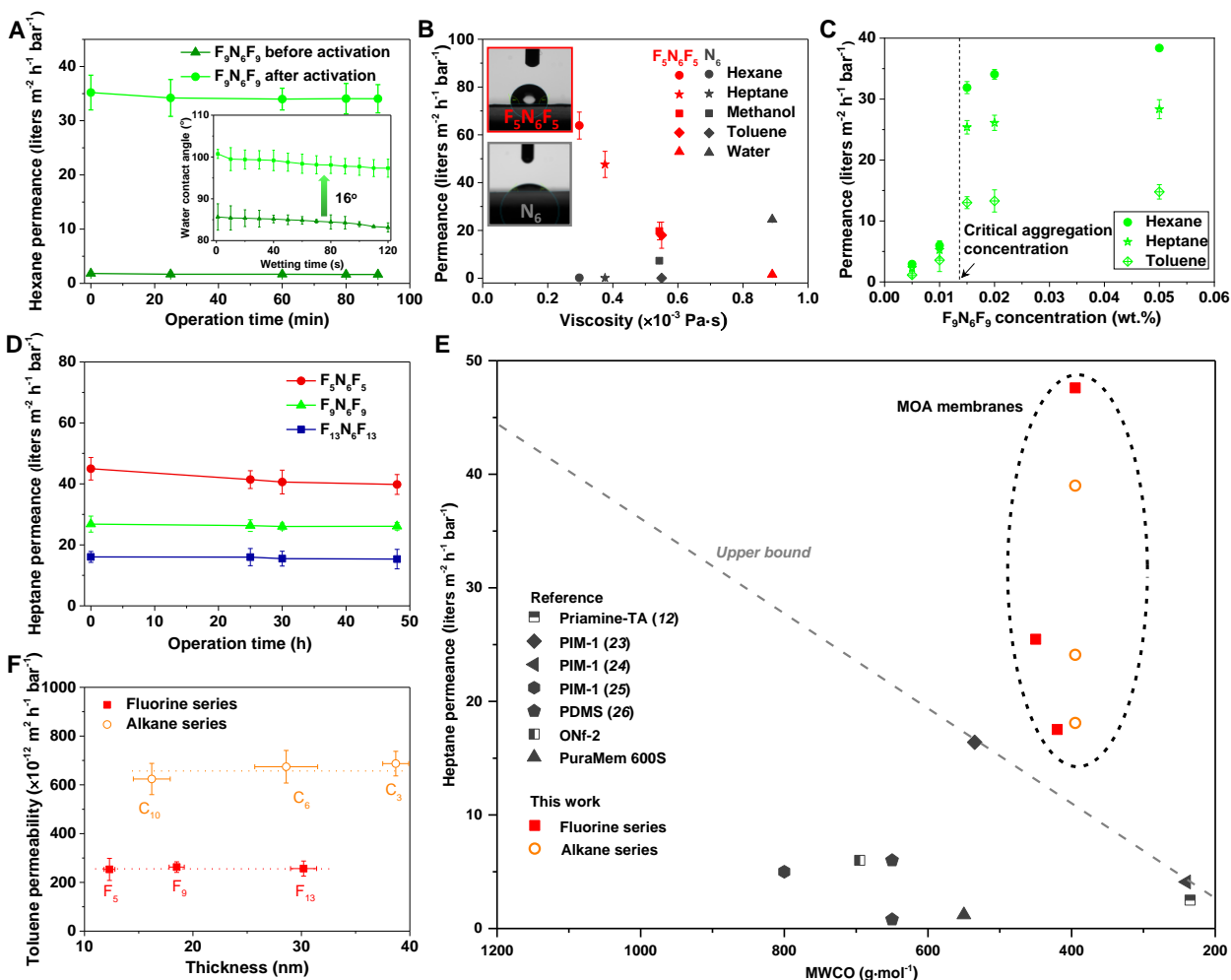
Fig. 3. Performance of nanofilms made from MOAs on polyacrylonitrile (PAN) supports. (A) Hexane permeance for membranes made from 0.02 wt.% $F_9N_6F_9$ before and after acetone activation. The inset shows the corresponding water contact angles. **(B)** Plot of solvent permeances through membranes made from 0.02 wt.% $F_5N_6F_5$ and its precursor amine, pentaethylenehexamine (N_6), against the solvent viscosity, where both membranes were tested after acetone activation. The inset shows the water contact angle for both membranes. **(C)** Non-polar solvent permeances including hexane, heptane, and toluene for $F_9N_6F_9$ membranes with increasing MOA concentrations. **(D)** Plot of heptane permeance against time for $F_5N_6F_5$, $F_9N_6F_9$, and $F_{13}N_6F_{13}$ membranes operating in a continuous crossflow rig. **(E)** Comparison of heptane permeance and

molecular weight cut-offs for polystyrene markers between MOA membranes (this work) and membranes reported in the literature. **(F)** Toluene permeability of membranes made from fluorine series ($F_5N_6F_5$, $F_9N_6F_9$, and $F_{13}N_6F_{13}$) and alkane series ($C_3N_6C_3$, $C_6N_6C_6$, and $C_{10}N_6C_{10}$) of MOAs. The error bars represent the standard deviation, which was calculated based on the results from three separate membranes.

We hypothesize that the close proximity of hydrophobic chains in these vesicles provides rapid transport pathways for non-polar liquids through the nanofilm. Further, MOA membranes could be activated by acetone to increase permeance. We assert that acetone activation re-arranges the hydrophobic blocks so that some of the initially inward-facing hydrophobic tails inside the vesicles extend from the outer surface (fig. S12). Activated $F_9N_6F_9$ membrane provided an order of magnitude higher hexane permeance compared to the membrane before activation (Fig. 3A). This corresponded to an increase of water contact angle from 82° to 98° after activation (Fig. 3A inset), consistent with exposure of the hydrophobic blocks (*11*). The net effect is creation of hydrophobic expressways for non-polar solvents, similar to the ultrafast water transport through aquaporin membranes (*21*). While conventional polyamide membranes exhibited enhanced permeance for all solvents after activation by dimethylformamide (DMF), MOA membranes showed a significant enhancement only for non-polar solvents (figs. S29 and S30). Moreover, MOA membranes after DMF activation exhibited ~8 times lower relative increase in permeance than that activated by acetone (fig. S31). Seeking to further explain this phenomenon, we examined the surface morphology, thickness, and the elemental composition of nanofilms before and after solvent activation (figs. S19, S21 and S28), and observed no significant differences. Therefore, we attribute the permeance boost to an increase in hydrophobicity arising from the rearrangement of hydrophobic blocks at a molecular level upon acetone exposure.

To demonstrate the impact of hydrophobic oligomers, the precursor amine without oligomers, pentaethylenehexamine (N_6), was employed to prepare hydrophilic polyamide nanofilms under identical conditions. This nanofilm was smooth, with no vesicles observed on the surface (fig. S19). Composite membranes comprising N_6 nanofilms showed no permeance increase after activation (fig. S32), exhibiting negligible permeances for non-polar solvents, but showed high permeance for polar solvents including water (Fig. 3B and table S1). By contrast, membranes incorporating MOA vesicles reversed this trend, demonstrating fast transport for non-polar solvents (Fig. 3B and fig. S33). For example, the hexane permeance reached 63.9 ± 5.6 liters m^{-2} hour^{-1} bar^{-1}, which is >100 times higher than that of N_6 membranes and other conventional hydrophilic polyamide membranes (*9*). This is consistent with the enhanced hydrophobicity of the MOA nanofilm, where the water contact angle increased from 42° for the N_6 membrane to 93° for the $F_5N_6F_5$ membrane (Fig. 3B inset).

To further evaluate the impact of vesicles, nanofilms were prepared with varying MOA concentrations (Fig. 3C and fig. S34). Below the CAC, no vesicles were formed in the aqueous phase, and the surface of the resulting nanofilms was relatively smooth (fig. S17), since the heat from the vigorous crosslinking reaction was efficiently dissipated through the bulk aqueous solution at the free interface (*22*). These pre-CAC membranes exhibited limited permeance increase after activation (fig. S35), with toluene permeance of 1.2 ± 0.3 liters m^{-2} hour^{-1} bar^{-1} recorded. This increased to 14.8 ± 1.2 liters m^{-2} hour^{-1} bar^{-1} for membranes incorporating vesicles made using MOA concentrations above the CAC (Fig. 3C), despite thinner nanofilms and similar crosslinking degree for the pre-CAC membranes (fig. S21 and S27). While the permeance dramatically increased, the rejection performance remained unchanged (fig. S36).

One advantage of MOA membranes is the potential to manipulate their performance by tuning the oligomer length or chemistry. Heptane permeance increased as the fluorine chain length shortened from $F_{13}N_6F_{13}$ to $F_5N_6F_5$ (Fig. 3D), due to the thinner separating layer created (Fig. 2H). The permeances remained constant over 48 hours, indicating no collapse of vesicles under 10 bar applied pressure (fig. S37). Polystyrene oligomers and dimer were dissolved in heptane to investigate their separation performance. The molecular weight cut-offs ranged from 395 to 450 g mol^{-1}, which is consistent with their dye rejections in methanol (fig. S38 and table S2). A trade-off between heptane permeance and molecular weight cut-off of polystyrene is plotted to compare the performance among MOA membranes, the commercial benchmarks, ONf-2 and PuraMem 600S, and other membranes reported in literature (Fig. 3E and table S3) (*12, 23-26*). MOA membranes exhibited separation performance well beyond the upper bound.

By tuning the chemistry of oligomers, composite membranes comprising a series of alkane MOA nanofilms were fabricated. Fig. 3F shows the toluene permeability for MOA membranes comprising both fluorine and alkane series. Within the same series, the toluene permeability remained unaltered, independent of the nanofilm thickness (Fig. 2H and fig. S27). Across different series, membranes made from the alkane MOAs provided more than double the permeability of the fluorine MOAs, without compromising the rejection (fig. S38). This illustrates that the oligomer chemistry in MOAs can tailor the permeance/permeability of the resulting membranes, suggesting that MOA membranes with designable oligomer functionality could be developed for dedicated separation tasks (*27*).
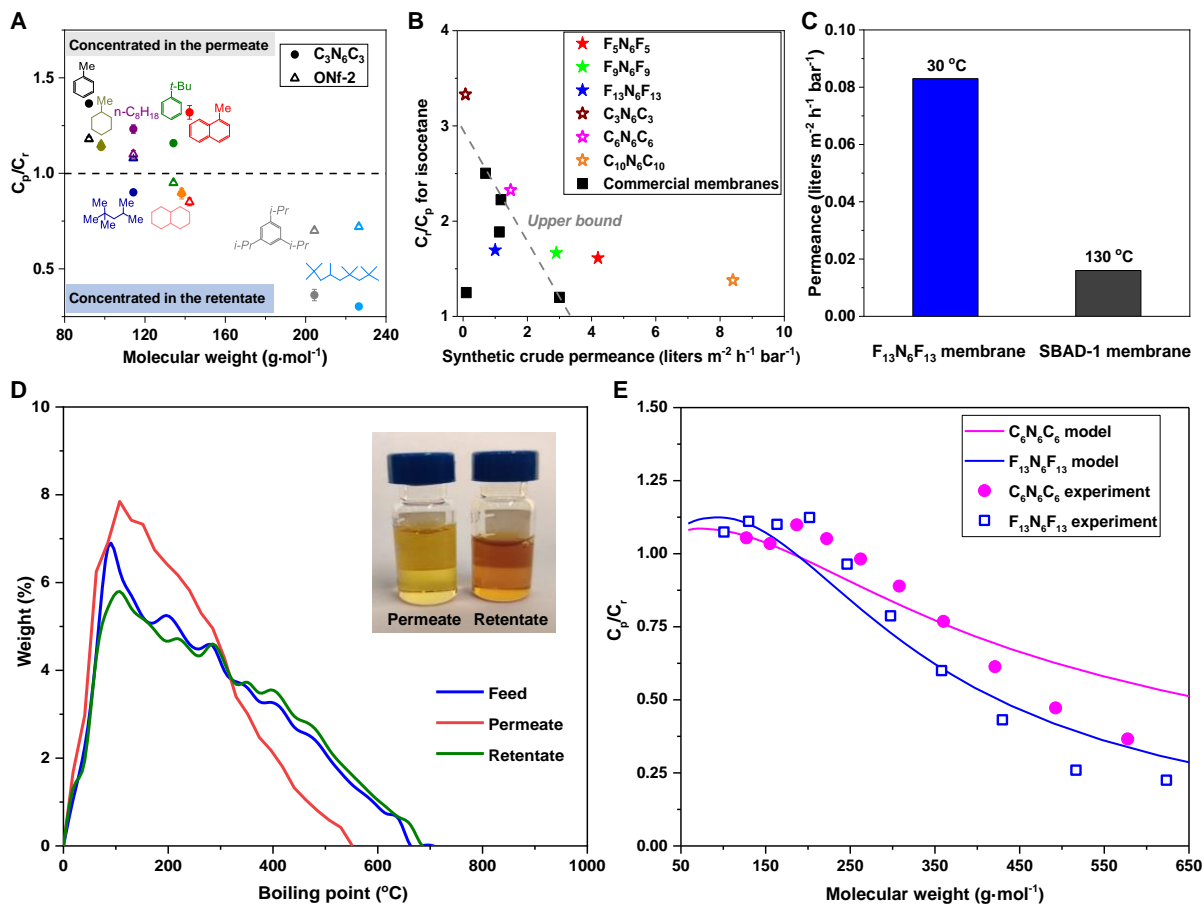
Fig. 4. Separation of synthetic and real crude oil using nanofilm composite membranes made from MOAs. (A) Ratio of concentrations in permeate (C_p) versus retentate (C_r) of components in a synthetic crude oil fractionated by $C_3N_6C_3$ membrane and commercial benchmark, ONf-2 membrane (40 bar, 22 °C, crossflow conditions). Molecules above the reference dash line were more concentrated in the permeate compared with the feed, whereas the molecules below the reference dash line were more concentrated in the retentate. **(B)** Comparison between membranes comprising MOAs ($F_5N_6F_5$, $F_9N_6F_9$, $F_{13}N_6F_{13}$, $C_3N_6C_3$, $C_6N_6C_6$, and $C_{10}N_6C_{10}$) and commercial membranes tested under the same conditions (40 bar, 22 °C, crossflow conditions), measured as C_r/C_p for iso-cetane (226.5 g mol^{-1}) and synthetic crude oil permeance. **(C)** Permeance of real light shale-based crude oil for $F_{13}N_6F_{13}$ membrane at 30 °C and SBAD-1 membrane at 130 °C, adapted

from ref. 5. **(D)** Boiling point distribution of feed, permeate, and retentate from $F_{13}N_6F_{13}$ membrane fractionation of light shale-based crude oil. Inset image shows permeate (left) and retentate (right) solutions. **(E)** Comparison of C_p/C_r extracted from experimental simulated distillation curve of permeate and retentate to model predictions for $C_6N_6C_6$ membranes and

5      $F_{13}N_6F_{13}$ membranes.

The ultrafast transport of non-polar solvents and the material tunability make MOA membranes a promising candidate for fractionation of small hydrocarbon liquid molecules. Challenging the MOA membranes with a synthetic crude oil composed of a group of hydrocarbon molecules in a crossflow filtration system (fig. S39 and table S4), we found they demonstrated

10   good separation of molecules based on differences in size and class (Fig. 4A). In contrast to conventional binary separation systems such as polystyrenes in heptane, there is no designated solvent or solute in complex crude oil mixture fractionation. Thus, the membrane selectivity is presented as the ratio of permeate to retentate concentrations (C_p/C_r) for each component plotted against the molecular weight of the components. After more than 24 hours of continuous operation,

15   membranes made from MOAs, especially $C_3N_6C_3$ membranes, demonstrated much better size- and class-based selectivity compared to ONf-2 membrane which is the current commercial benchmark used for processing hydrocarbon liquids (Fig. 4A, fig. S40, and table S5). We speculate that the flexible alkane chains of $C_3N_6C_3$ in the membrane have a strong interaction with "structure-like" hydrocarbon molecules, resulting in the retention of the larger species (*5, 27*). Moreover, when

20   elevating the system temperature from 22 °C to 50 °C, $C_3N_6C_3$ membranes displayed good thermal stability and increased permeance, without compromising the selectivity, while ONf-2 membranes showed decreasing selectivity at high temperature (fig. S41). Fig. 4B shows the trade-off between permeance and selectivity of the largest molecule, iso-cetane, for membranes tested with the

synthetic crude oil. The performance of most MOA membranes exceeded the upper bound compared to that of commercial membranes (table S6). This is due to the ultrathin MOA nanofilms formed via interfacial polymerization (*22*), enabling faster transport than commercial membranes with thick separating layers formed by phase inversion (*7*).

5　　　MOA membranes were further challenged with a real light shale-based crude oil. For this process, SBAD-1 membrane is the current state-of-the-art membrane with the highest permeance reported in literature (*5, 6*). Fig. 4C demonstrates that the permeance of the $F_{13}N_6F_{13}$ membrane was more than 5 times higher than that of SBAD-1 membrane even operating at room temperature (30 °C), while high temperature (130 °C) was needed for the SBAD-1 membrane to achieve
10　　comparable selectivity (*5*). This is attributed to the ultrathin thickness of nanofilms fabricated by interfacial polymerization, whereas hundreds of nanometers thick active layers were formed in the SBAD-1 membrane through spin coating technique. The enhanced liquid permeance can significantly reduce the required membrane area, plant footprint and hence the capital cost for any specific refinery capacity (*16*). Fig. 4D shows the boiling point distribution of the feed, permeate,
15　　and retentate from the light shale-based crude. The permeate has a cut-off at 550 °C while the feed and retentate boiling point range extends to 700 °C. This demonstrates that the membrane rejects the heavy (residue) fraction of the crude oil. At the same time, the permeate was found to be appreciably enriched in the lighter molecules present in the feed, so that more than 60 wt.% of the permeate had a boiling point below 400 °C compared to 48 wt.% observed in the feed. A GC×GC
20　　difference plot for the permeate and retentate samples further demonstrated that the permeate was lighter than the retentate, with high concentrations of light saturates and light aromatic molecules in the permeate while there is rejection of heavier 3- and 4-ring aromatics (fig. S42). These results highlight the capabilities of MOA membranes in crude oil fractionation, providing enrichment of

high-value light molecules and rejection of low-value heavy molecules while exhibiting the high permeances that industrial application demands. To demonstrate the scalability of this approach, conventional interfacial polymerization was carried out to fabricate in-situ MOA membranes directly on the support (fig. S43). They showed satisfying separation performance in synthetic crude oil (fig. S44), which reinforces the potential for using these materials in large scale industrial applications.

To understand the origin of the high selectivity using MOA membranes in hydrocarbon separation systems, a modelling approach based on diffusion theory is proposed in Supplementary Section 3. The model allows for the representation of membrane based fractionation of crude oil on the basis of a single parameter and it was applied to separations using fluorine and alkane oligomers (tables S7 and S8). The model gives a good fit of the light shale based crude oil separation data with the experimental results for fluorine series ($F_{13}N_6F_{13}$ membranes) and alkane series ($C_6N_6C_6$ membranes), both having a cross-over at molecular weight of ~200 g mol^{-1} (Fig. 4E). $F_{13}N_6F_{13}$ membranes show a better retention for large hydrocarbon molecules than $C_6N_6C_6$ membranes, which is consistent with permeate boiling point cut-off results at 10% stage cut, 550 °C for $F_{13}N_6F_{13}$ membranes and 590 °C for $C_6N_6C_6$ membranes (fig. S45 and table S8). The increased retention of heavy species with $F_{13}N_6F_{13}$ membranes results from the low solubility of hydrocarbons in fluoropolymers (*28*).

By using MOAs for interfacial polymerization, we have fabricated ultrathin hydrophobic polyamide nanofilm membranes incorporating vesicles from the self-assembled MOAs. In processing hydrocarbon liquids, these membranes are more permeable, selective, and stable than commercially available and other literature reported membranes. We also highlight the feasibility of manipulating the crude oil separation performance at molecular level by introducing oligomers

—

with different chemistries into the MOA molecules. This work facilitates the development of the next-generation hydrophobic nanofilms created via interfacial polymerization, incorporating rational molecular level design and with the potential for scaling up.

References and Notes

- D. S. Sholl, R. P. Lively, Seven chemical separations to change the world. *Nature* **532**, 435-438 (2016).

- M. Elimelech, W. A. Phillip, The future of seawater desalination: Energy, technology, and the environment. *Science*. **333**, 712–717 (2011).

- D.Y. Koh, B. A. McCool, H. W. Deckman, R. P. Lively, Reverse osmosis molecular differentiation of organic liquids using carbon molecular sieve membranes. *Science* **353**, 804-807 (2016).

- R. P. Lively, D. S. Sholl, From water to organics in membrane separations. *Nat. Mater.* **16**, 276–279 (2017).

- K. A. Thompson et al., N-Aryl–linked spirocyclic polymers for membrane separations of complex hydrocarbon mixtures. *Science* **369**, 310-315 (2020).

- S. Chisca et al., Polytriazole membranes with ultrathin tunable selective layer for crude oil fractionation. *Science* **376**, 1105-1110 (2022).

- P. Marchetti, M. F. Jimenez Solomon, G. Szekely, A. G. Livingston, Molecular separation with organic solvent nanofiltration: A critical review. *Chem. Rev.* **114**, 10735–10806 (2014).

- M. F. Jimenez-Solomon, Q. Song, K. E. Jelfs, M. Munoz-Ibanez, A. G. Livingston, Polymer nanofilms with enhanced microporosity by interfacial polymerization. *Nat. Mater.* **15**, 760 (2016).

- S. Karan, Z. Jiang, A. G. Livingston, Sub-10 nm polyamide nanofilms with ultrafast solvent transport for molecular separation. *Science* **348**, 1347-1351 (2015).

- M. F. Jimenez Solomon, Y. Bhole, A. G. Livingston, High flux hydrophobic membranes for organic solvent nanofiltration (OSN)—Interfacial polymerization, surface modification and solvent activation. *J. Membr. Sci.* **434**, 193–203 (2013).

- J. S. Trivedi, P. Bera, D. V. Bhalani, S. K. Jewrajka, In situ amphiphilic modification of thin film composite membrane for application in aqueous and organic solvents. *J. Membr. Sci.* **626**, 119155 (2021).

- S-H. Park et al., Hydrophobic thin film composite nanofiltration membranes derived solely from sustainable sources. *Green Chem.* **23**, 1175-1184 (2021).

- F. Alduraiei, P. Manchanda, B. Pulido, G. Szekely, S. P. Nunes, Fluorinated thin-film composite membranes for nonpolar organic solvent nanofiltration. *Sep. Purif. Technol*. **279**, 119777 (2021).

- F. Alduraiei, S. Kumar, J. Liu, S. P. Nunes, G. Szekely, Rapid fabrication of fluorinated covalent organic polymer membranes for organic solvent nanofiltration. *J. Memb. Sci.* **648**, 120345 (2022).

- W. Kushida, et al. Organic solvent mixture separation using fluorine-incorporated thin film composite reverse osmosis membrane. *J. Mater. Chem. A* **10,** 4146-4156 (2022).

- J. F. Brennecke, B. Freeman, Reimagining petroleum refining. *Science* **369**, 254-255 (2020).

- F. Aydin, Self-assembly and critical aggregation concentration measurements of ABA triblock copolymers with varying B block types: model development, prediction, and validation. *J. Phys. Chem. B.* **120**, 3666-3676 (2016).

- W. Tao et al., A linear-hyperbranched supramolecular amphiphile and its self-assembly into vesicles with great ductility. *J. Am. Chem. Soc.* **134**, 762–764 (2012).

- Y. Ma, X. Cao, X. Feng, Y. Ma, H. Zou, Fabrication of super-hydrophobic film from PMMA with intrinsic water contact angle below 90°. *Polymer* **48**, 7455–7460 (2007).

- M. D. Vincenzo et al., Biomimetic artificial water channel membranes for enhanced desalination. *Nat. Nanotechnol.* **16**, 190–196 (2021)

- K. Murata et al., Structural determinants of water permeation through aquaporin-1. *Nature* **407**, 599-605 (2000).

- Z. Jiang, S. Karan, A. G. Livingston, Water transport through ultrathin polyamide nanofilms used for reverse osmosis. *Adv. Mater.* **30** (2018).

- P. Gorgojo et al., Ultrathin polymer films with intrinsic microporosity: Anomalous solvent permeation and high flux membranes. *Adv. Funct. Mater.* **24**, 4729-4737 (2014).

- D. Fritsch, P. Merten, K. Heinrich, M. Lazar, M. Priske, High performance organic solvent nanofiltration membranes: Development and thorough testing of thin film composite membranes made of polymers of intrinsic microporosity (PIMs). *J. Membr. Sci*. **401–402**, 222–231 (2012).

- M. Cook, P. R. J. Gaffney, L. G. Peeva, A. G. Livingston, Roll-to-roll dip coating of three different PIMs for Organic Solvent Nanofiltration. *J. Membr. Sci.* **558**, 52–63 (2018).

- M. Cook, L. Peeva, A. G. Livingston, Solvent-Free Coating of Epoxysilicones for the Fabrication of Composite Membranes. *Ind. Eng. Chem. Res.* **57**, 730–739 (2018).

- H. L. Castricum et al., Tailoring the Separation Behavior of Hybrid Organosilica Membranes by Adjusting the Structure of the Organic Bridging Group. *Adv. Funct. Mater.* **21**, 2319-2329 (2011).

- B. D. Marshall, J. W. Allen, & R. Lively, A Model for the Separation of Complex Liquid Mixtures with Glassy Polymer Membranes: A Thermodynamic Perspective. Available SSRN 3976709.

- R. Taylor, & R. Krishna, *Multicomponent mass transfer*. vol. 2 (John Wiley & Sons, 1993).

- R. Mathias, et al. Framework for predicting the fractionation of complex liquid feeds via polymer membranes. J. Memb. Sci. 640, 119767 (2021).

- M. R. Riazi, Characterization and properties of petroleum fractions (Vol. 50). ASTM international (2005).

- N. von Solms, M. L. Michelsen, & G. M. Kontogeorgis, Computational and physical performance of a modified PC-SAFT equation of state for highly asymmetric and associating mixtures. Industrial & Engineering Chemistry Research, 42(5), 1098–1105 (2003).

- P. K. Jog, S. G.Sauer, J. Blaesing, & W. G. Chapman, Application of dipolar chain theory to the phase behavior of polar fluids and mixtures. Industrial & Engineering Chemistry Research, 40(21), 4641–4648 (2001).

- J. Gross & G. Sadowski, Perturbed-chain SAFT: An equation of state based on a perturbation theory for chain molecules. Industrial & Engineering Chemistry Research, 40 (4), 1244–1260 (2001).

- B. D. Marshall & C. P. Bokis, A PC-SAFT model for hydrocarbons II: General model development. Fluid Phase Equilibria, 478, 34–41 (2018).

Acknowledgments:

Funding:

Author contributions:

S. L. and R. D. synthesized multiblock oligomer amines. S. L. performed NMR analysis, FT-IR analysis, measured water contact angle, captured SEM and AFM images. V. M. captured TEM images. N. D. R., J. R. J., S. H. and B. A. M. tested membrane performance in real crude oil system, performed boiling point measurement, and GC×GC analysis. B. D. M performed model development and application. S. L. fabricated composite membranes and performed OSN experiments. Z. J. tested membranes in synthetic crude system. J. K. built up the synthetic crude testing rig and tested the commercial membrane performance in synthetic crude system. S. C. performed XPS test. S. L., R. D., N. D. R., J. R. J., J. X., B. A. M., S. P. N., Z. J. and A. G. L. conceived the research. All authors contributed to drafting the paper.

Competing interests:

Authors declare no competing interests.

Data and materials availability:

All data is available in the main text or the supplementary materials.

Supplementary Materials

Materials and Methods

Supplementary Text

Figs. S1 to S45

Tables S1 to S8

Theoretical analysis of light shale crude oil separation data

Movie

References (*29-35*)

Science

AAAS

Supplementary Materials for

Hydrophobic Polyamide Nanofilms Provide Rapid Transport for Crude Oil Separation

Siyao Li[1], Ruijiao Dong[1,2], Valentina-Elena Musteata[3], Jihoon Kim[1,4,7], Neel D. Rangnekar[5], J. R. Johnson[5], Bennett D. Marshall[5], Stefan Chisca[3], Jia Xu[1,6], Scott Hoy[5], Benjamin A. McCool[5], Suzana P Nunes[3], Zhiwei Jiang[1,7]*, Andrew G. Livingston[1,7]*

Affiliations:
[1]Barrer Center, Department of Chemical Engineering, Imperial College London, South Kensington Campus, London SW7 2AZ, UK.
[2]Shanghai Center for Systems Biomedicine, Key Laboratory of Systems Biomedicine, Shanghai Jiao Tong University, Shanghai 200240, China.
[3]King Abdullah University of Science and Technology, Biological and Environmental Science and Engineering Division, Advanced Membranes and Porous Materials Center, Thuwal, Saudi Arabia.
[4]Process Design and Research Center, Chemical and Process Technology Division, Korea Research Institute of Chemical Technology, Daejeon, 34114, South Korea.
[5]Corporate Strategic Research, ExxonMobil Research and Engineering, Annandale, NJ 08801, USA.
[6]Key Laboratory of Marine Chemistry Theory and Technology (Ministry of Education), School of Materials Science and Engineering, College of Chemistry and Chemical Engineering, Ocean University of China, Qingdao, 266100, China
[7]Department of Engineering and Materials Science, Queen Mary University of London, Mile End Road, London E1 4NS, UK.

Correspondence to: zhiwei.jiang@qmul.ac.uk; a.livingston@qmul.ac.uk

This PDF file includes:
Materials and Methods
Figs. S1 to S45
Tables S1 to S8
Theoretical analysis of light shale crude oil separation data
Captions for Movies S1

Other Supplementary Materials for this manuscript include the following:
Movies S1

Materials and Methods

Materials

1,1'-Carbonyldiimidazole (CDI), 1H,1H-Nonafluoro-1-pentanol, 1H,1H-Tridecafluoro-1-heptanol and 2,2,3,3,3-Pentafluoro-1-propanol were purchased from Tokyo chemical industrial UK Ltd. Trimesoyl chloride (TMC) 98%, pentaethylenehexamine (PEHA) with technical grade, 2-naphthalenemethanol, 1-Heptanol, 1-Undecanol, 1-Butanol, 2,4-Diphenyl-4-methyl-1-pentene, 1-Methylnaphthalene, n-Octane, tert-Butylbenzene, 1,3,5-Triisopropylbenzene, 2,2,4,4,6,8,8-Heptamethylnonane, Methylcyclohexane and 2,2,4-Trimethylpentane were purchased from Sigma-Aldrich. Polystyrene (nominal Mp 1000 g mol^{-1}), Polystyrene (nominal Mp 580 g mol^{-1}) were purchased from Agilent Technologies, Inc. Commercial ONf-2 membrane was purchased from BORSIG Membrane Technology GmbH. Commercial Puramem Performance, Puramem Flux, Puramem Selective, and Puramem 280 manufactured by Evonik MET Ltd were purchased from Sterlitech, USA. All solvents used for phase inversion, interfacial polymerization and nanofiltration experiments were purchased from VWR, UK. All the reagents and solvents mentioned above were used without any further purification.

Multiblock oligomer amines (MOAs) synthesis

Synthesis of F$_5$N$_6$F$_5$

2,2,3,3,3-Pentafluoro-1-propanol (7.75 g) and CDI (8.314 g, 1.0 equiv.) were dissolved in dimethylformamide (DMF) (40 mL) in a round-bottom flask with strong magnetic stirring. The reaction took place at 40 °C using an oil bath under argon atmosphere. After stirring for 3 hours, PEHA (5 g, 0.42 equiv.) was added to the mixture and the reaction was left overnight. The colour of the reaction mixture changed from colourless to light yellow. After cooling to room temperature, the reaction mixture was slowly added to an excess of hexane and dichloromethane (DCM) mixture under strong magnetic stirring. The resulting yellow precipitate was collected by separation funnel and re-dissolved in DCM (100 mL). A semi-saturated saline (300 mL) was used for extraction. The supernatant was removed while the underlying layer was extracted again with saturated saline. The procedure was repeated three times to remove water soluble by-products. The remaining small amount of water was removed by anhydrous sodium sulphate collected with filter paper. Excess solvent was removed by rotary evaporator and the product further dried under high vacuum at 150 °C. The resulting product was collected and dried to give the title compound as a yellow gel (7.36 g, 58.5% yield).

Synthesis of F$_9$N$_6$F$_9$

F$_9$N$_6$F$_9$ was synthesized following a similar procedure as above: 1H,1H-Nonafluoro-1-pentanol (3.874 g) and CDI (2.512 g, 1.0 equiv.) were mixed in DMF (20 mL) and stirred at 40 °C for 3 hours. PEHA (1.5 g, 0.42 equiv.) was added, followed by continuous stirring for another 12 hours. The resulting mixture was concentrated to 10 mL under vacuum and precipitated in 200 mL hexane and DCM (90%/10% volume ratio). The precipitate was collected and rinsed with hexane three times. The precipitate was re-dissolved in 100 mL DCM for extraction. 300 mL semi-saturated saline water was added. The mixture was shaken well. The supernatant was removed while the underlying layer was extracted again by semi-saturated saline. The procedure was repeated three

times to remove water soluble by-products. The collected solution containing desired product was dried to give the title compound as a yellow gel (2.92 g, 58%).

Synthesis of $F_{13}N_6F_{13}$

The synthesis procedure for $F_{13}N_6F_{13}$ was as follows: A DMF solution (45 mL) containing 1H,1H-Tridecafluoro-1-heptanol (10.85 g) and CDI (5.02g, 1.0 equiv.) were stirred under argon at 40 °C for 3 hours. Then a specific amount of mixed PEHA (3 g, 0.42 equiv.) was added, followed by continuous stirring for another 12 hours at 40 °C. The resulting reaction mixture was precipitated in 500 mL hexane, the precipitate was then collected and washed with hexane three times. The precipitate was dissolved in DCM (100 mL) and extracted with 300 mL 80% saturated saline three times. The solution was collected and dried to give the title compound as a yellow gel (6.93 g, 54.5%).

Synthesis of $C_3N_6C_3$

$C_3N_6C_3$ was synthesized by mixing n-butanol (3.83 g) and CDI (8.37 g, 1.0 equiv.) in DMF (40 mL) and the mixture was stirred at 50 °C under argon for 4 hours. PEHA (5.0 g, 0.45 equiv.) was subsequently added, and the resulting solution stirred at the same temperature for 12 hours. After concentrating the mixture, it was dissolved in 100 mL DCM and subsequently extracted with 300 mL 80% saturated saline three times. The organic phase was collected, and DCM was evaporated by rotary evaporator. The obtained mixture was dissolved in 5 ml DCM, followed by adding to 400 mL hexane drop-by-drop. The precipitate was collected and rinsed with hexane three times. The resulting precipitate was collected and dried to give the title compound as a yellow gel (5.88 g, 63.2%).

Synthesis of $C_6N_6C_6$

$C_6N_6C_6$ was synthesized by mixing heptanol (6 g) and CDI (8.37 g, 1.0 equiv.) in DMF (40 mL) and the mixture was stirred at 50 °C under argon for 3 hours. PEHA (5.0 g, 0.42 equiv.) was subsequently added, and the resulting solution was stirred at the same temperature for 12 hours. After concentrating the mixture, it was precipitated by adding to 400 mL hexane drop- by-drop. The precipitate was collected and subsequently dissolved in DCM (100 mL) and extracted with 300 mL 80% saturated saline three times. The collected solution containing desired product was dried to give the title compound as a yellow gel (11.8 g, 85.1%).

Synthesis of $C_{10}N_6C_{10}$

A mixture of 1-undecanol (4.89 g) and CDI (4.6 g, 1.0 equiv.) in DMF (35 mL) was stirred under argon at 50 °C for 3 hours. Subsequently, PEHA (3.0 g, 0.45 equiv.) was added, and the resulting solution was stirred at 50 °C for 12 hours. After stripping off excess DMF, the residue was precipitated in 200 mL hexane, and the precipitate collected for extraction. The precipitate was re-dissolved in DCM (100 mL) followed by adding 300 mL 80% saturated saline in a separation funnel. After mixing mixture was allowed to separate for 0.5 hours, then supernatant was discarded while the underlying layer was extracted again by 80% saturated saline. The process was repeated 4 times. The resulting solution was collected and dried to give the title compound (5.72 g, 70.5%) as a brown solid gel.

Characterization techniques

Nuclear Magnetic Resonance (NMR)

5 1H NMR spectra was recorded on a Brüker AVANCE III-400 spectrometer, with working frequencies of 400 (1H) using Deuterated chloroform ($CDCl_3$) as a solvent at 293 K. Chemical shift of $CDCl_3$ is given in ppm relative to the signal corresponding to the residual $CHCl_3$: $CDCl_3$, $\delta H = 7.26$ ppm. Note: Prior to the NMR analysis, all solutions were passed through a pipette filled with cotton to remove the insoluble impurities and dust.

Scanning electron microscopy (SEM)

High resolution scanning electron microscopy (SEM, LEO 1525, Karl Zeiss) was used to characterize the surface and cross-sectional images of the nanofilms. The nanofilms were sputtered with 10 nm thick chromium coating (Q150T turbo-pumped sputter coater, Quorum Technologies Ltd.) under an argon atmosphere (2×10^{-2} mbar).

15

X-ray photoelectron spectroscopy (XPS)

X-ray photoelectron spectroscopy (XPS) studies were performed in a Kratos Axis Supra DLD spectrometer equipped with a monochromatic Al Kα X-ray source (h$\nu = 1486.6$ eV) operating at 150 W, under high vacuum (~10^{-9} mbar), using an aperture slot of 300 μm x 700 μm. Survey 20 spectra were collected using a pass energy of 160 eV and a step size of 1 eV. High resolution XPS spectra were carried out using a pass energy of 20 eV and a step size of 0.1 eV.

Transmission Electron Microscopy (TEM)

TEM imaging of thin polyamide films, film cross-section and self-assembled oligomer vesicles 25 was conducted on a FEI Titan-CT microscope operating at 300 kV. To prepare the samples for the self-assembled vesicles, a drop of solution was placed onto a lacey carbon-coated copper grid, blotted with filter paper and dried at ambient conditions. The polyamide interfacial thin films were picked up on the copper TEM grids and transmission images across the film were acquired. To analyze the thin film cross-section, the freestanding nanofilms were transferred onto 30 polyacrylonitrile supports and small pieces were stained with ruthenium tetroxide to enhance the electronic contrast. Then, the membranes were embedded in epoxy resin, and cured overnight at 65 °C. Thin sections (100 nm) were cut with an ultramicrotome, collected on 300 mesh copper grids and imaged by TEM. High Angle Annular Dark Field Scanning TEM (HAADF-STEM) and Energy-Dispersive X-ray Spectroscopy TEM (EDX-TEM) mapping of thin films were conducted 35 on a FEI Themis Z TEM.

Atomic force microscopy (AFM)

The thickness of the nanofilm was measured using ICON (Bruker, CA, USA) atomic force microscope (AFM) with E type scanner. Free-standing nanofilms were transferred onto silicon 40 wafers and dried at room temperature. A scratch was made to expose the wafer surface, so that the height difference between the silicon wafer surface and the nanofilm surface revealed the nanofilm thickness. A resolution of 512 points per line was used. Gwyddion 2.44 SPM software was used to process the AFM images.

Water contact angle

Water contact angle was measured with a KRÜSS drop-shape analyser. Prior to testing, each membrane sample was thoroughly rinsed with methanol to remove the residual acyl chloride, followed by air drying at room temperature overnight. A syringe with a blunt end dispensing tip was used to deliver the water droplet onto the membrane surface. The contact angle was continuously recorded for 2 min with a frequency of 5 measurements per second using a digital camera.

Fourier-transform infrared spectroscopy (FTIR)

Fourier transform infrared (FTIR) spectra were recorded on a Perkin-Elmer Spectrum 100 spectrometer between wavenumbers of 4000-650 cm^{-1}. The instrument was equipped with a Universal ATR sampling accessory (diamond crystal), with a red laser excitation source (633 nm), and a middle infrared (MIR) triglycine sulphate (TGS) detector.

Dynamic light scattering (DLS)

The vesicle size was measured by DLS using Malvern Zetasizer Nano S. The test temperature was set at 25 °C and a quartz cuvette was used for size measurement. The results were recorded with a frequency of 5 measurements for 3 runs.

Membrane fabrication and performance test

Fabrication of polyacrylonitrile (PAN) support via phase inversion

The PAN support was fabricated via a non-solvent phase inversion method. A polymer dope solution was prepared by dissolving the PAN powder at 11 wt.% in a solvent mixture comprising DMSO/1,4-dioxane at a weight ratio of 1:1, followed by stirring at 200-300 rpm at 85°C using an overhead stirrer overnight. The dope solution was firstly filtered through polytetrafluoroethylene (PTFE) filter paper (40 μm) at 5 bar, and then filtered again using PTFE filter paper (11 μm) at the same pressure, to remove undissolved polymer. Ultrasonication was used for degassing for at least 1 hour until no air bubbles could be seen, then the dope solution was ready for casting. The PAN membrane was cast on a continuous casting machine with polyethylene terephthalate (PET) nonwoven (Hirose RO grade) by phase inversion of 30 s at a blade thickness of 120 μm. The PAN was then placed in water at 60 °C for 3h. Constant temperature was needed to obtain the desired pore size. After casting, the membranes went through multiple exchanges with water and were then allowed to air-dry.

Fabrication of thin film composite (TFC) membrane

The free-standing polyamide film was formed at an aqueous-organic interface. The aqueous phase was prepared by firstly dissolving 0.02 g MOA in tetrahydrofuran (THF) (5 g). Subsequently, adding the de-ionized water (5 g) dropwise under strong magnetic stirring, followed by pouring another 90 g de-ionized water into the solution. The interface was created by the aqueous phase containing multiple oligomer amines and a hexane phase containing TMC in a glass petri dish.

After reacting for 7 minutes, the nanofilms were picked up using a stainless-steel plate, followed by floating them onto a water surface for relaxation in a large glassware container. The nanofilms were then transferred onto various supports to incorporate them into thin film composite membranes for organic solvent nanofiltration experiments, or onto substrates for characterization.

Nanofiltration performance test

Nanofiltration performance of the composite membranes was evaluated by determining permeance profiles and molecular weight cut off (MWCO) curves. Nanofiltration experiments involving dye separations were carried out under 10 bar at 25 °C in a dead-end cell, and nanofiltration experiments involving polystyrene separations were carried out at 10 bar at 25 °C using a crossflow filtration system. For each filtration experiment in the dead-end cell, one membrane disc, of active area 12.6 cm^2, was cut out from flat sheets and placed into the cell, and at least three membranes made under identical conditions were used to demonstrate the reproducibility.

Permeate samples for permeance measurement were collected at intervals of 10 min, and samples for rejection evaluation were taken after steady permeance was achieved. The MWCO was determined by interpolating from the plot of rejection against molecular weight of dye compounds. Each rejection test comprised one dye solute with a constant concentration of 20 mg L^{-1} in methanol. Analysis of dye concentrations was done using an UV-vis detector in the wavelength ranging from 200 to 800 nm. The concentration and hence the rejection was calculated based on the absorption values at the characteristic wavelength of dyes. For crossflow filtration, the membrane discs, of active area 13.8 cm^2, were cut out from flat sheets and placed into 4 cross flow cells in series. Permeate samples for permeance measurements were collected at intervals of 4h, and samples for rejection evaluations were taken after steady permeate flux was achieved. The permeance (P) was calculated as following:

$$P = \frac{V}{A \times \Delta t \times \Delta p} \tag{1}$$

where V is the volume of permeate collected (liters), A is the area of the membrane (m^2), Δt is the time elapsed for collecting the required permeate volume (hour), ΔP is the transmembrane pressure (bar). The unit of the permeance was liters per square meter per hour per bar (liters m^{-2} hour^{-1} bar^{-1}) which is the conventional standard.

The rejection (R) was determined as following:

$$R = 1 - \frac{C_p}{C_f} \tag{2}$$

Where C_p is the concentration of permeate and C_f is the concentration of feed.

The MWCO was determined by interpolating from the plot of rejection against molecular weight of marker compounds. The solute rejection test was carried out using a standard feed solution comprised of a homologous series of styrene oligomers (PS) dissolved in the selected solvent. The styrene oligomer mixture contained 1g L^{-1} each of PS 580 and PS 1000 (Agilent, UK), and 0.1 g L^{-1} of α-methylstyrene dimer (Sigma-Aldrich, UK). Analysis of the styrene oligomers was done using an Agilent HPLC system with UV-vis detector set at a wavelength of 264 nm. Separation was achieved using a reverse phase column (C18-300, 250×4.6 mm). The mobile phase consisted of 10 vol% analytical grade water and 90 vol% THF.

Synthetic crude oil separation test

Synthetic crude oil separation experiments were carried out under 40 bar at 25 °C and 50 °C in a crossflow filtration system (fig. S39). The flow rate was set at 100 ml min^{-1}. The temperature of the system was adjusted by immersing a spiral coil heater into oil bath, and heated by the heating plate. The membrane discs, of active area 13.8 cm^2, were cut out from flat sheets and placed into 3 crossflow cells in series. Permeate samples for permeance measurements were collected at intervals of 6 h. Gas chromatography was used to analyze the hydrocarbon species.

Light Shale-based crude oil test

Separation of a light shale-based crude oil was carried out in a Sterlitech HP4750X dead-end cell. A coupon of $F_{13}N_6F_{13}$ membrane with active area of 14.8 cm^2 was cut out from flat sheets and placed into the cell. Initially, 200 ml each of water, acetone and toluene (in that order) were filtered through the membrane at room temperature and 10 bar. Following this "activation" procedure, the cell was charged with 100 g of a light shale-based crude oil. Using nitrogen head pressure, the crude oil feed was pressurized to 43 bar and maintained at room temperature (22 °C). The cell was stirred at a constant rate of 400 rpm. The weight of permeate (converted to volume (V)) was measured as a function of time (t) and using the membrane active area (A) and transmembrane pressure (ΔP), the average membrane permeance (P) was calculated according to Equation (1). The permeate, feed and retentate samples were analyzed using a standardized simulated distillation technique to determine their boiling point distributions and a standard two-dimensional gas chromatography technique to visualize separation based on class and molecular weight.

Supplementary tables and figures

1. Characterization of MOAs and the formation of self-assembly MOA vesicles

1.1 Chemical structure of multiblock oligomer amines
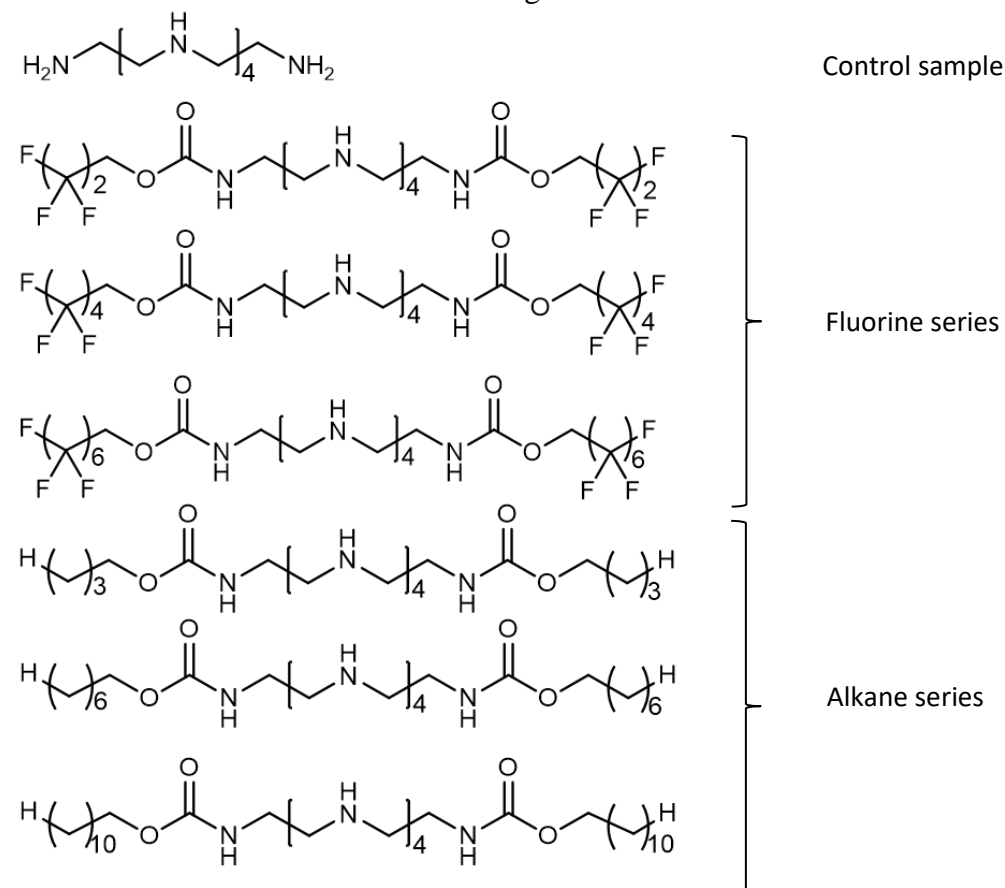
Fig. S1. Chemical structures of control sample pentaethylenehexamine (N_6) and MOAs. N_6 is the precursor used to synthesize MOAs.

1.2 Nuclear magnetic resonance (NMR) spectroscopy of MOAs
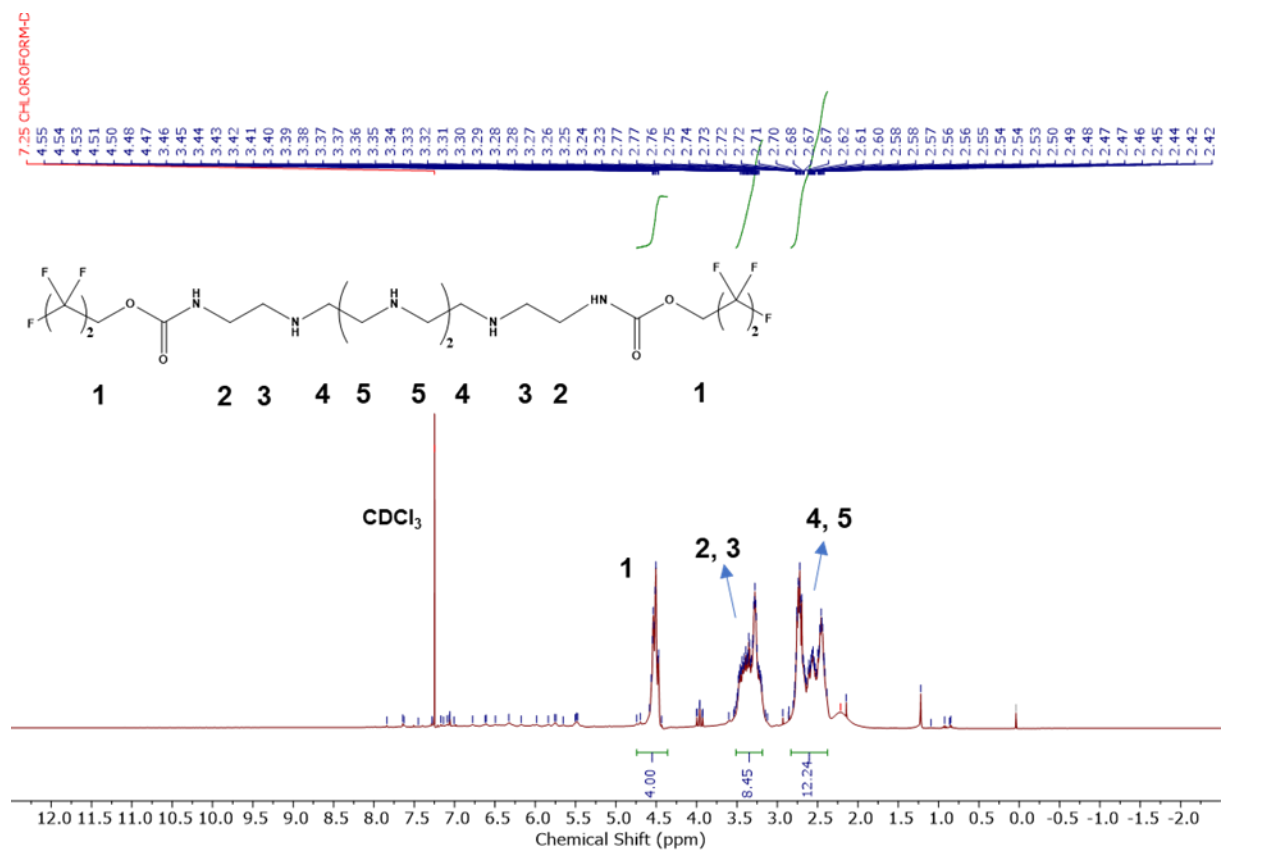
¹**H NMR (400 MHz, CDCl₃)** δ_H = 4.51 (dt, 4H, 2×CH_2O(CO)NH₂), 3.27 (m, 8H, 2×CH₃O(CO)NHCH_2CH_2NH₂), 2.61 (m, 12H, 3×CH_2CH_2NH₂).

Fig. S2. 1H NMR spectrum of $F_5N_6F_5$ in CDCl₃.
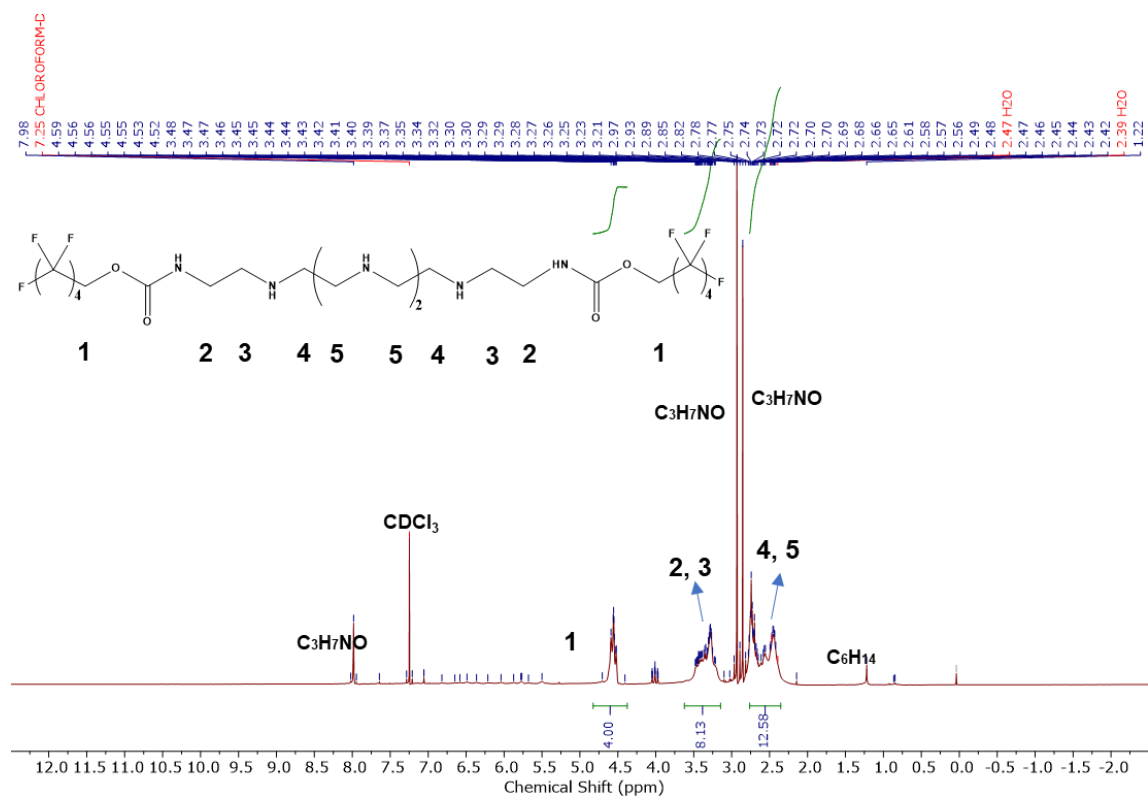
¹H NMR (400 MHz, CDCl₃) δ_H = 4.51 (dt, 4H, 2×C**H₂**O(CO)NH₂), 3.27 (m, 8H, 2×CH₃O(CO)NHC**H₂**C**H₂**NH₂), 2.61 (m, 12H, 3×C**H₂**C**H₂**NH₂).

Fig. S3. 1H NMR spectrum of F₉N₆F₉ in CDCl₃.
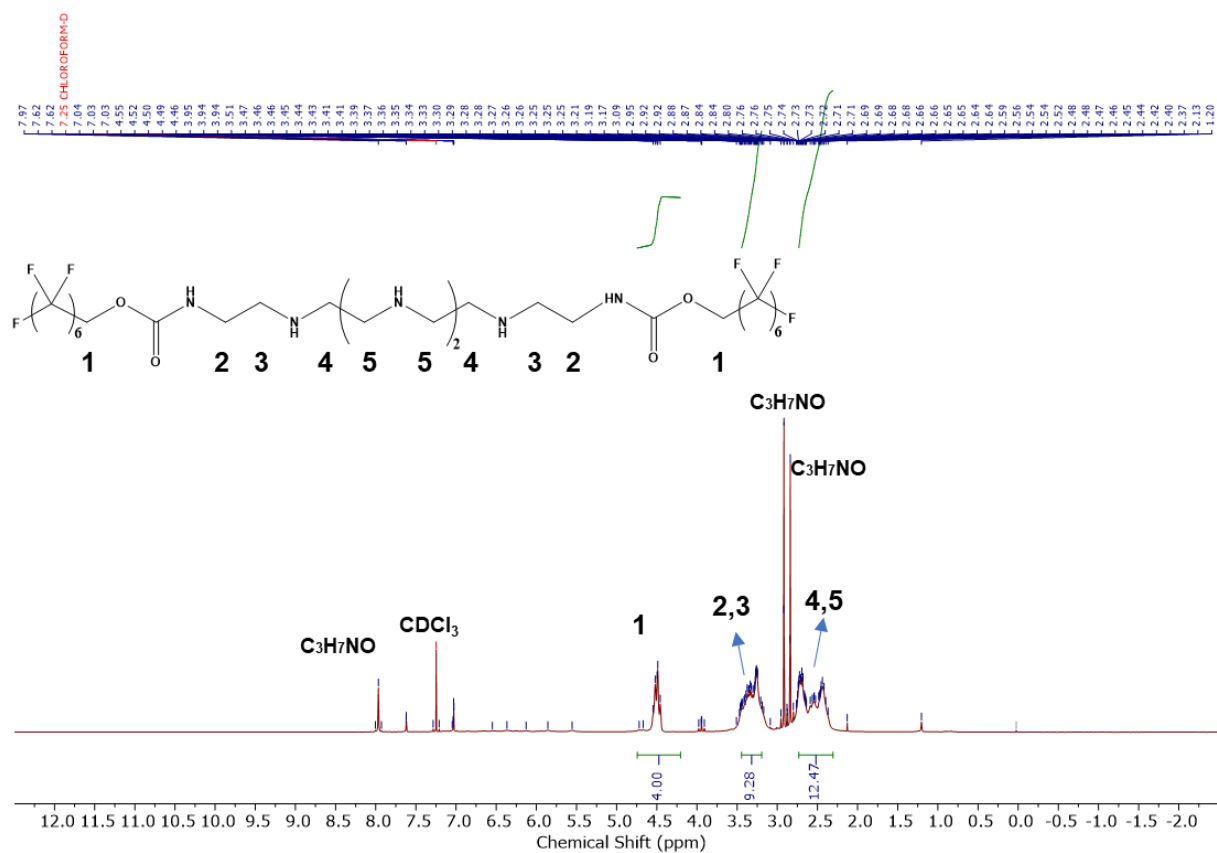
¹H NMR (400 MHz, CDCl₃) δ_H = 4.51 (dt, 4H, 2×C**H₂**O(CO)NH₂), 3.27 (m, 8H, 2×CH₃O(CO)NHC**H₂**C**H₂**NH₂), 2.61 (m, 12H, 3×C**H₂**C**H₂**NH₂).

Fig. S4. 1H NMR spectrum of $F_{13}N_6F_{13}$ in CDCl₃.
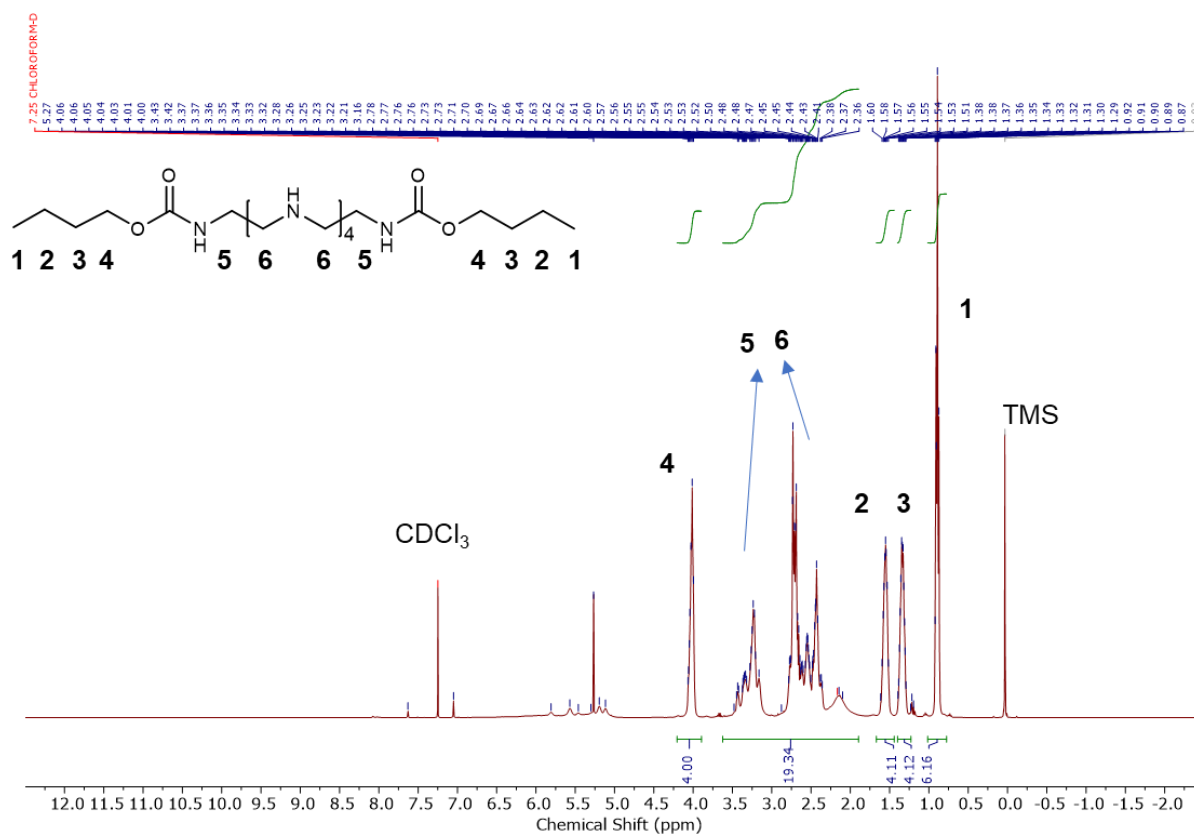
¹H NMR (400 MHz, CDCl₃) δ_H = 4.01 (dt, 4H, 2×C$\boldsymbol{H_2}$O(CO)NH₂), 3.27 (m, 8H, 2×C$\boldsymbol{H_2}$C$\boldsymbol{H_2}$NH₂), 2.61 (m, 12H, 3×C$\boldsymbol{H_2}$C$\boldsymbol{H_2}$NH₂), 1.57 (m, 4H, 2×C$\boldsymbol{H_2}$CH₃), 1.26 (m, 4H, 2× C$\boldsymbol{H_2}$CH₂CH3), 0.85 (m, 6H, 2×C$\boldsymbol{H_3}$).

5

Fig. S5. 1H NMR spectrum of C₃N₆C₃ in CDCl₃.
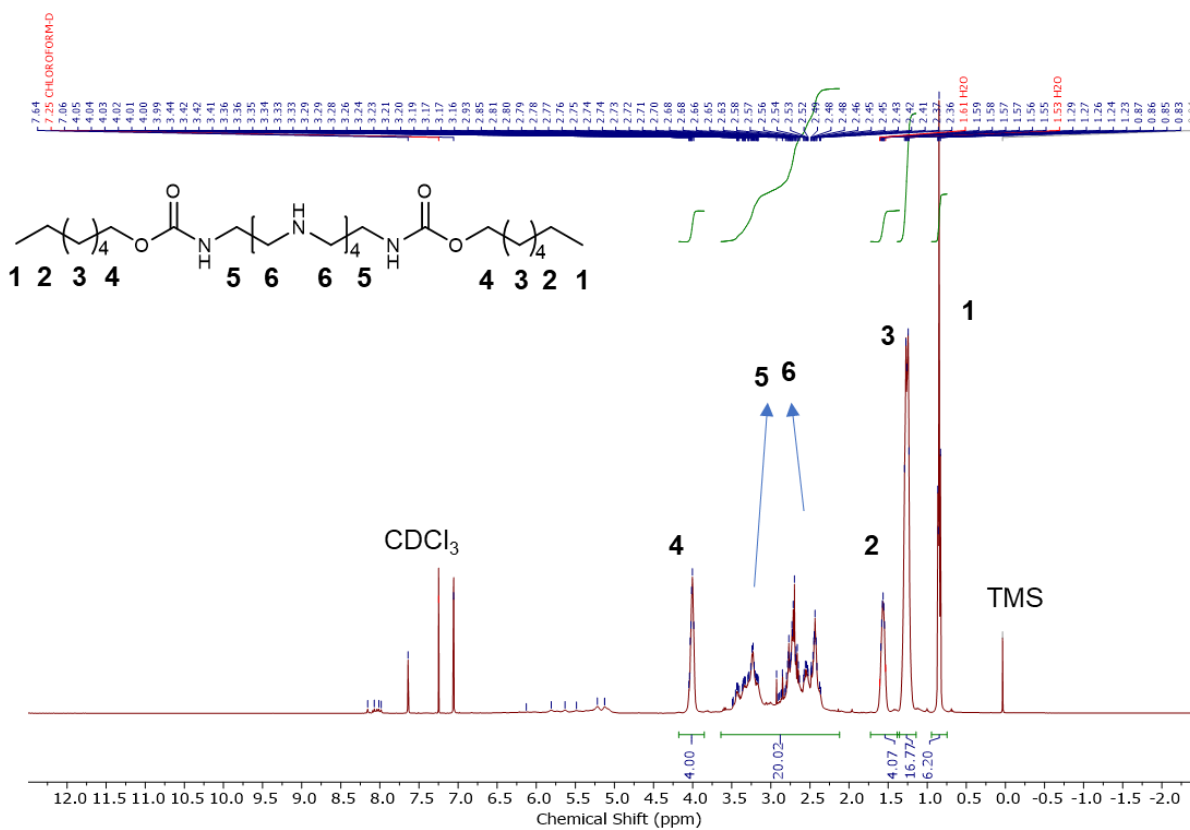
¹H NMR (400 MHz, CDCl₃) δ_H = 4.01 (dt, 4H, 2×C**H₂**O(CO)NH₂), 3.27 (m, 8H, 2×C**H₂**C**H₂**NH₂), 2.61 (m, 12H, 3×C**H₂**C**H₂**NH₂), 1.57 (m, 4H, 2×C**H₂**CH₃), 1.26 (m, 16H, 8× C**H₂**CH₂CH3), 0.85 (m, 6H, 2×C**H₃**).

5

Fig. S6. 1H NMR spectrum of C₆N₆C₆ in CDCl₃.
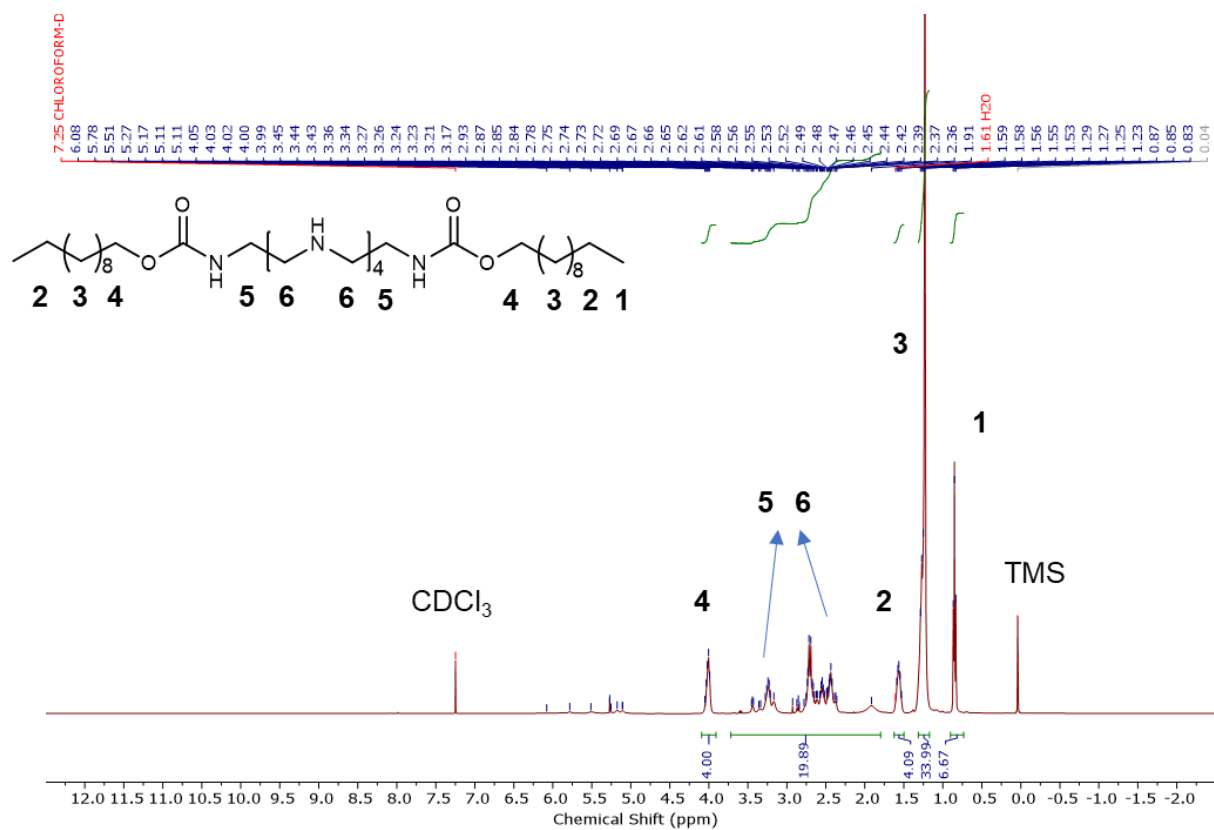
^{1}**H NMR (400 MHz, CDCl$_3$)** δ_H = 4.01 (dt, 4H, 2×C**H$_2$**O(CO)NH$_2$), 3.27 (m, 8H, 2×C**H$_2$**C**H$_2$**NH$_2$), 2.61 (m, 12H, 3×C**H$_2$**C**H$_2$**NH$_2$), 1.57 (m, 4H, 2×C**H$_2$**CH$_3$), 1.26 (m, 32H, 16× C**H$_2$**CH$_2$CH3), 0.85 (m, 6H, 2×C**H$_3$**).

Fig. S7. 1H NMR spectrum of C$_{10}$N$_6$C$_{10}$ in CDCl$_3$.

1.3 Fourier-transform infrared (FTIR) spectroscopy of MOAs with fluorine groups
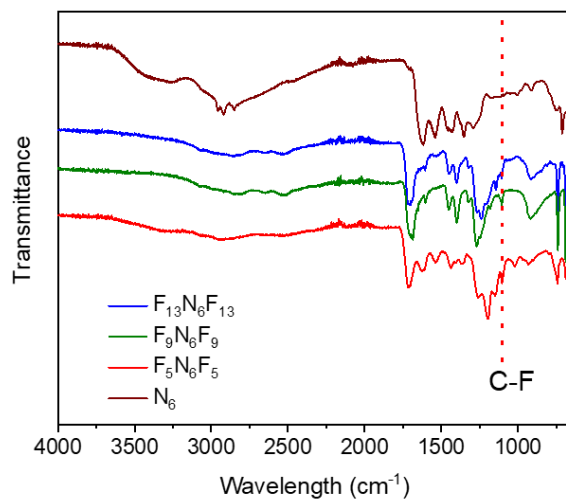
Fig. S8. FT-IR spectra of MOAs with fluorine series, including $F_5N_6F_5$, $F_9N_6F_9$ and $F_{13}N_6F_{13}$. Control sample N_6 was also included.

1.4 Critical aggregation concentration of MOAs

$CAC_{(F_5N_6F_5)} = 0.127$ mg/mL $= 0.218$ mM $\qquad$ $CAC_{(F_9N_6F_9)} = 0.132$ mg/mL $= 0.168$ mM

$CAC_{(F_{13}N_6F_{13})} = 0.149$ mg/mL $= 0.151$ mM $\qquad$ $CAC_{(C_3N_6C_3)} = 0.120$ mg/mL $= 0.286$ mM

$CAC_{(C_6N_6C_6)} = 0.146$ mg/mL $= 0.281$ mM $\qquad$ $CAC_{(C_{10}N_6C_{10})} = 0.162$ mg/mL $= 0.251$ mM
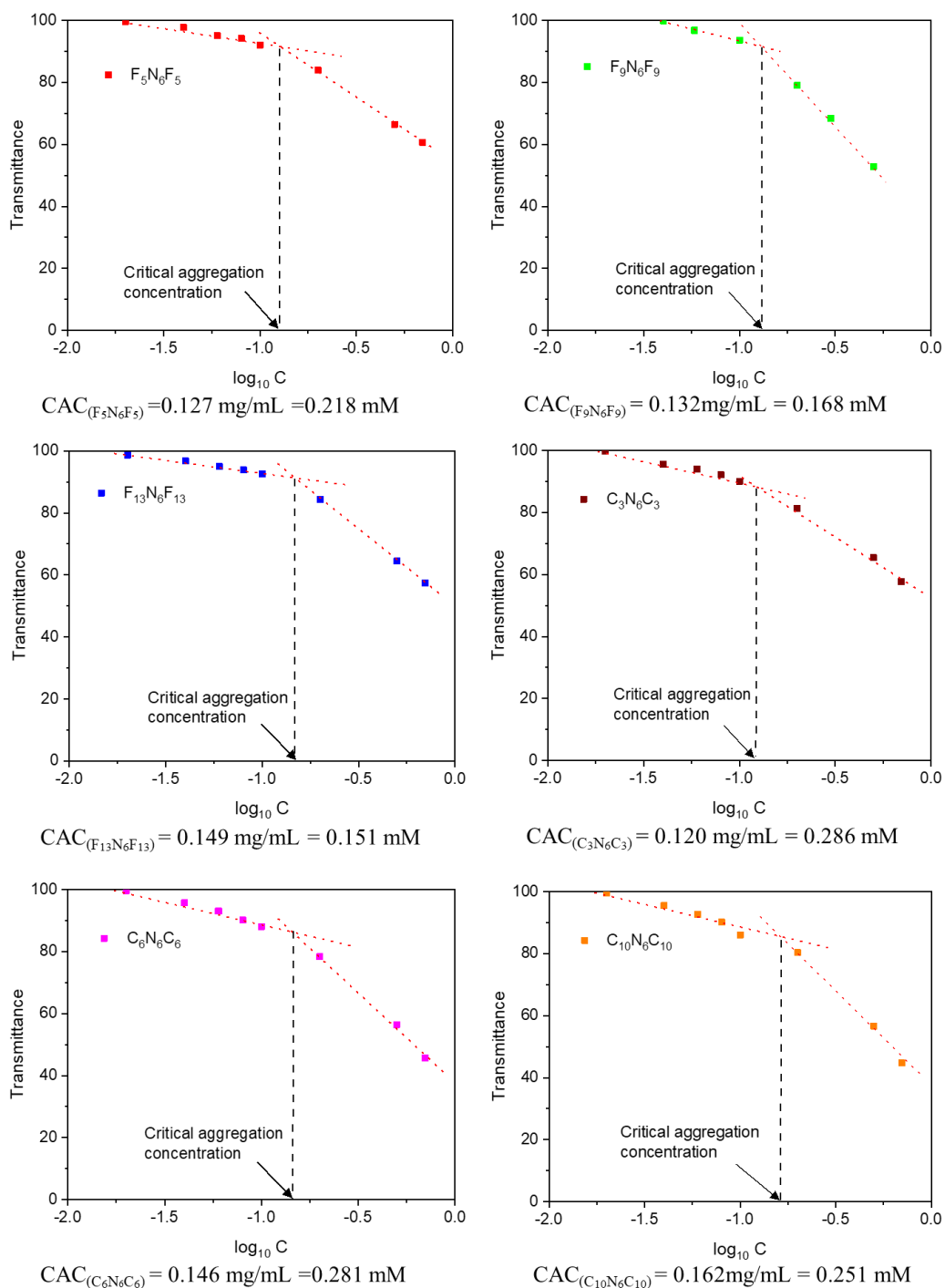
Fig. S9. Critical aggregation concentration (CAC) of MOAs. CAC was determined as the point at which light transmittance for the solution underwent a sudden decrease, indicating the formation of micelles or vesicles. Light transmission was measured by UV-vis spectrometer.
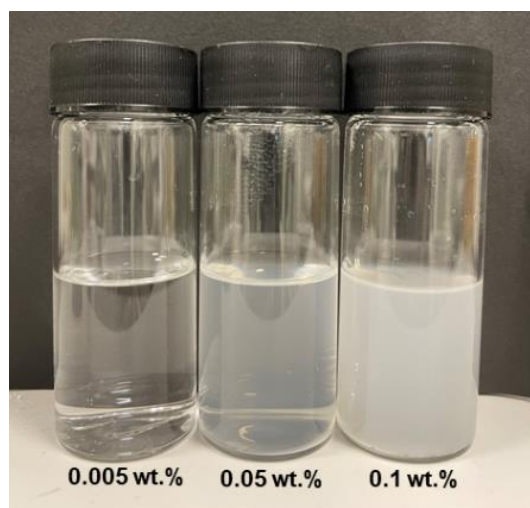
Fig. S10. Photograph of $F_5N_6F_5$ solutions with different MOA concentrations, including 0.005 wt.%, 0.05 wt.% and 0.1 wt.% in 5 wt.% / 95 wt.% THF/water mixture. The solutions were prepared by dissolving $F_5N_6F_5$ in THF, followed by adding an equivalent volume of water dropwise into the solution under strong stirring. Subsequently the rest of water required to reach 95% water / 5% THF was poured in and the solution was stirred for 20 minutes. With the concentration below CAC (i.e., C=0.005 wt.%), no micelles or vesicles formed, resulting in a clear solution. For concentrations above CAC (i.e., C=0.05 wt.% and 0.1 wt.%), the solutions became milky, indicating the formation of micelles or vesicles from self-assembly of MOAs.

1.5 Size distribution and morphology images of self-assembly MOA vesicles
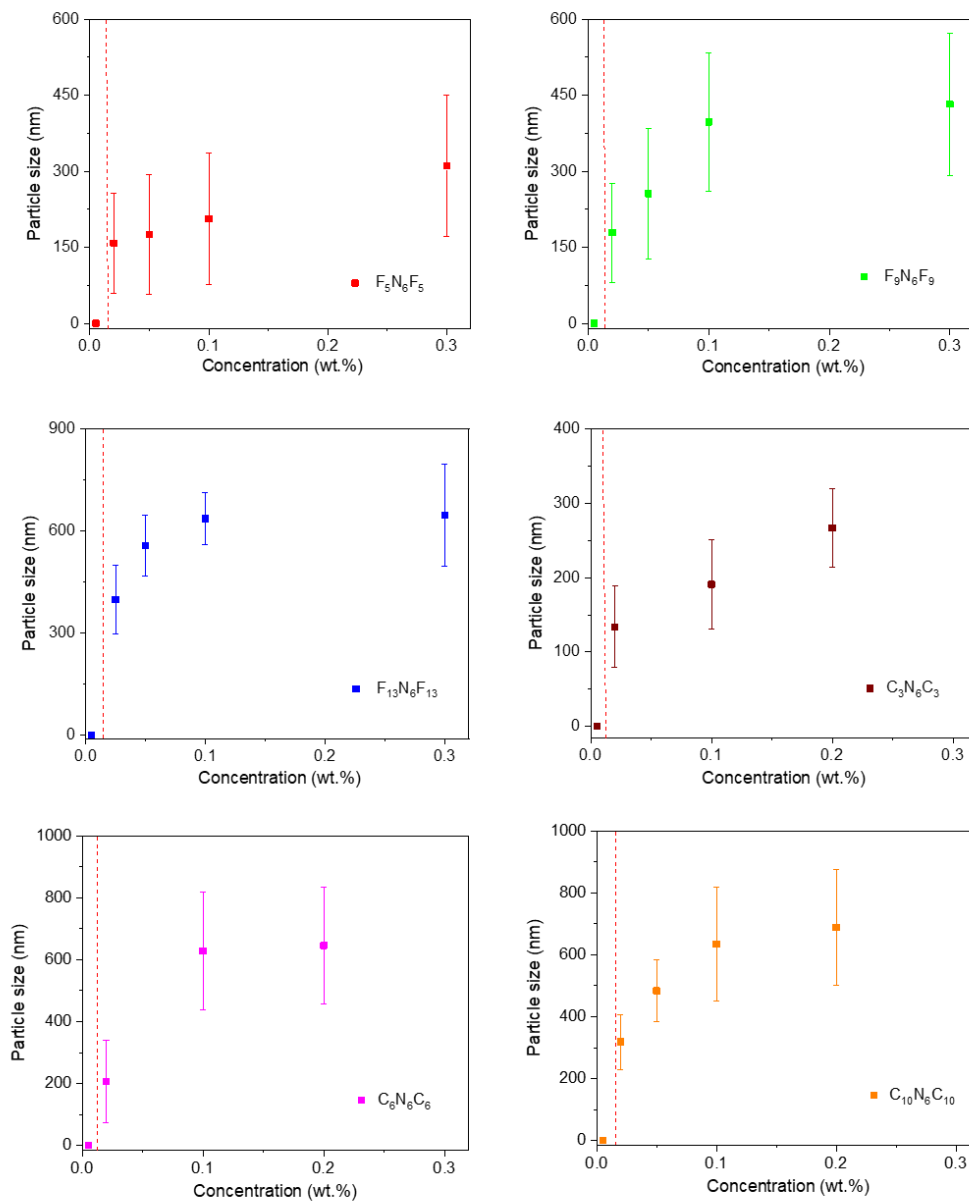
Fig. S11. Particle size of MOAs measured by dynamic light scattering (DLS). Micelles or vesicles formed by MOAs have a broad size distribution. The error bars represent the standard deviation, which was calculated based on the results of three samples.

A
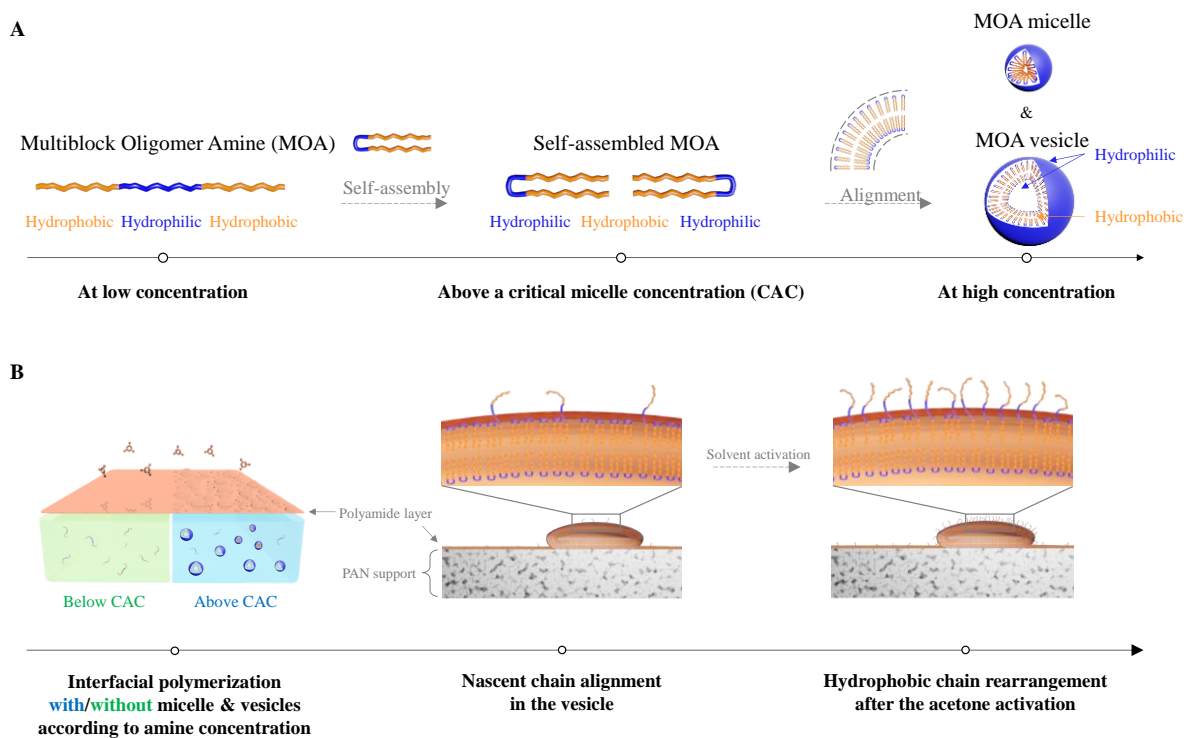
Fig. S12. Conceptual diagram at molecular level of (A) extended and self-assembled MOA at increasing concentration, and (B) polyamide nanofilms made with MOA before and after acetone activation.

5
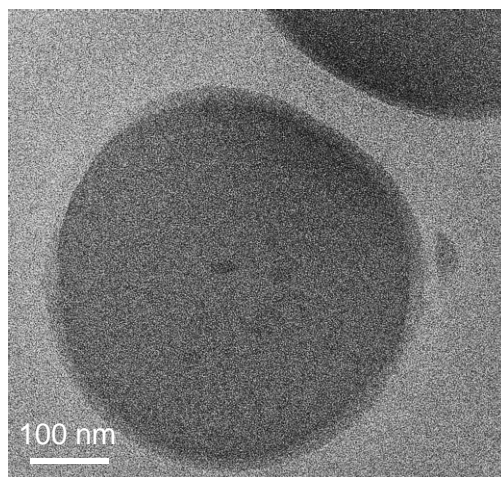
Fig. S13. TEM images of vesicles from self-assembly of $F_5N_6F_5$ molecules at 0.1 wt.% concentration.

10
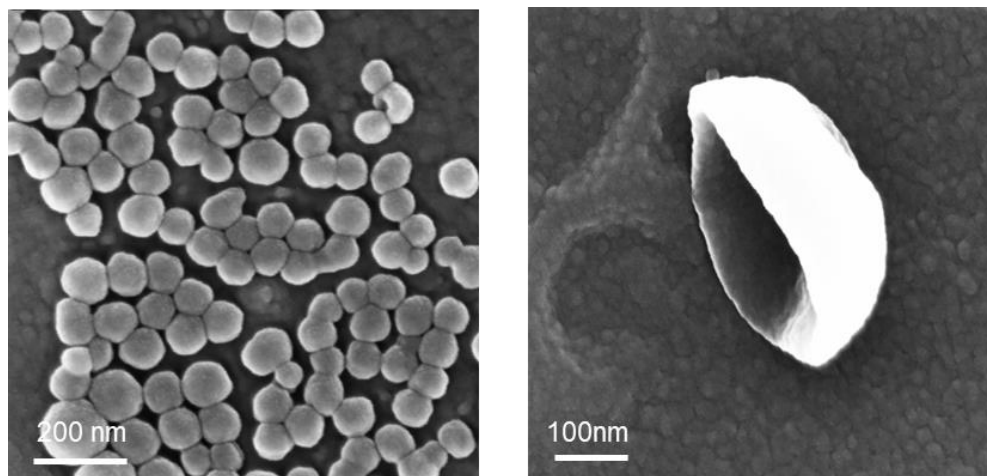
Fig. S14. SEM images of vesicles from self-assembly of $F_5N_6F_5$ at 0.1 wt.% concentration. The vesicle size is polydisperse and the inner hollow structure can be directly seen from vesicles interrupted by processing them for SEM analysis.

5

10

15

20

25

30

2. Fabrication and characterization of membranes

2.1 The fabrication of free-standing nanofilms and transfer to porous supports
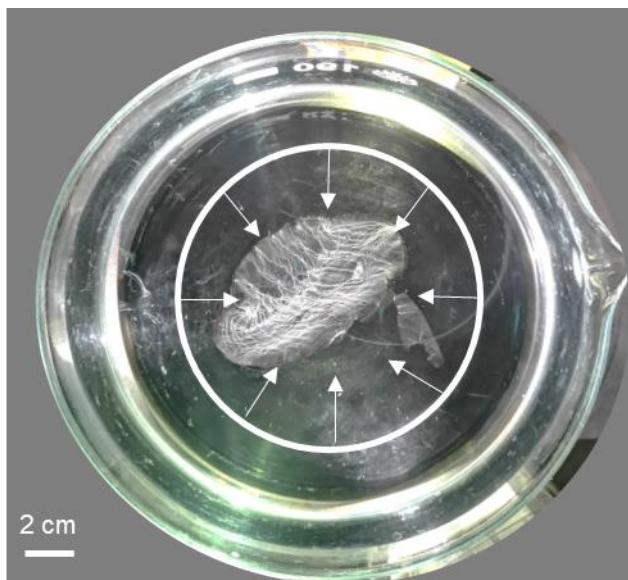
Fig. S15. Photograph of a $F_5N_6F_5$ nanofilm made at high MOA concentration (0.2 wt.%) transferred to a water surface. Nanofilms prepared from concentrated MOA solution shrank to a small area, due to their enhanced hydrophobicity, upon contact with water. Obvious wrinkles were observed on nanofilm surfaces. The white circle is original nanofilm disc size at the aqueous-organic interface.
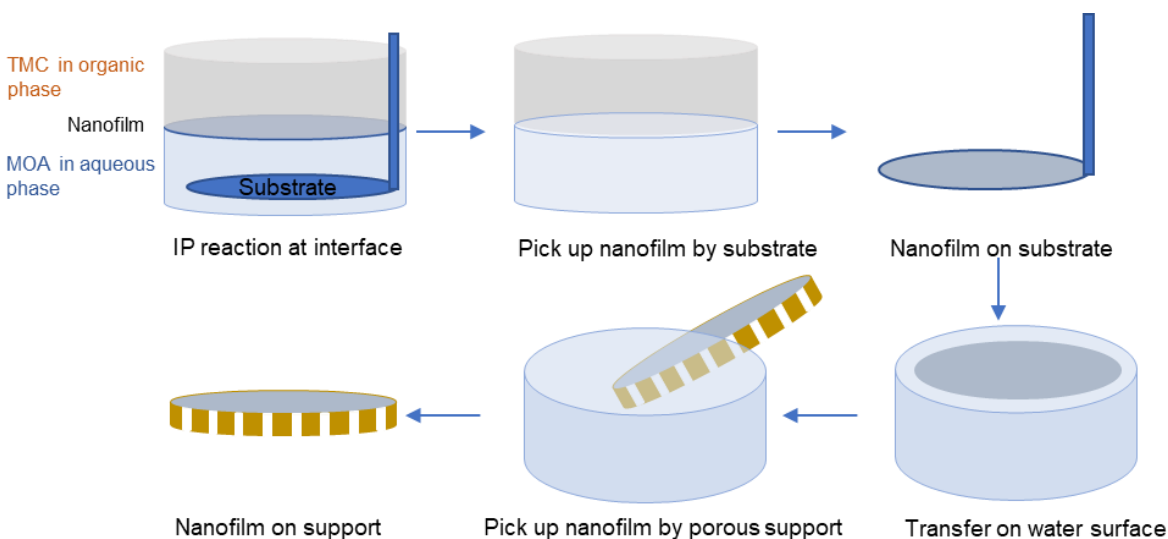
Fig. S16. Schematic illustrating interfacial polymerization at a free interface between an aqueous phase containing MOAs and a hexane phase containing trimesoyl chloride. The resulting nanofilm was picked up and transferred onto a porous support to form a thin film composite membrane.

2.2 Membrane characterization

A 0.002 wt.%

B 0.005 wt.%
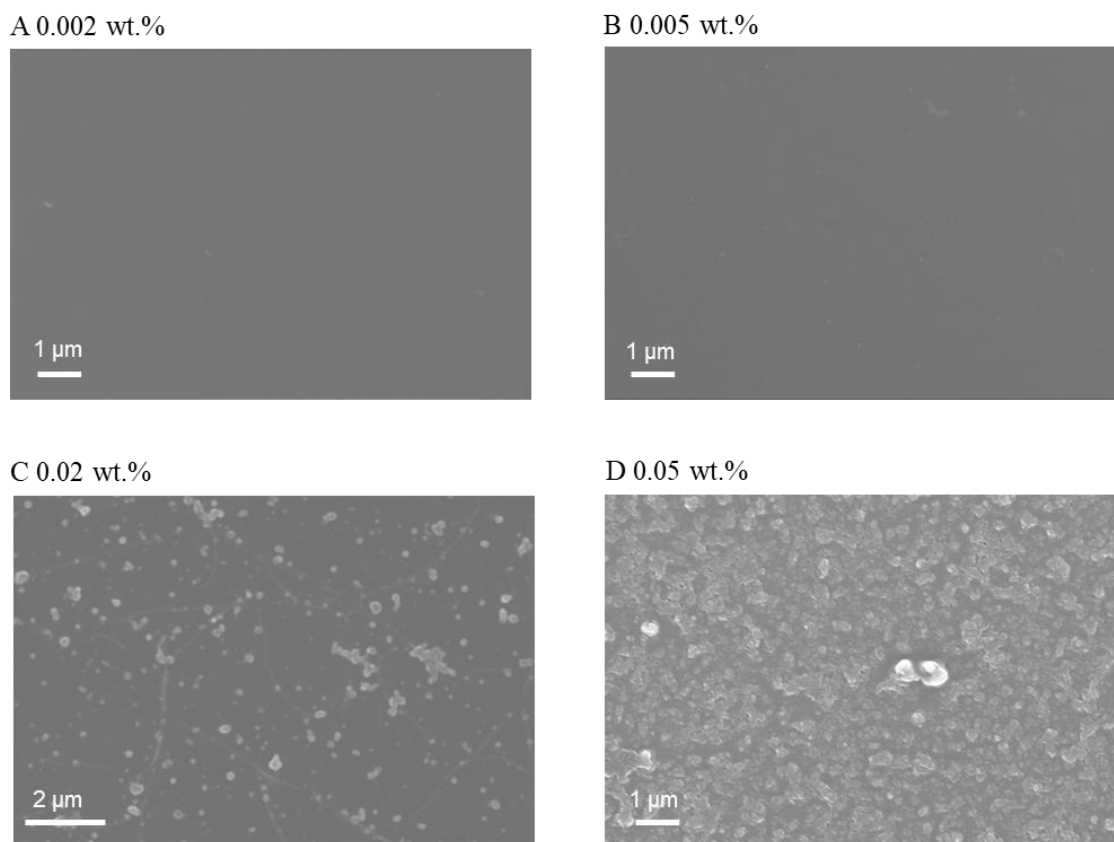
C 0.02 wt.%

D 0.05 wt.%

Fig. S17. SEM images of surface morphology of membranes made using $F_9N_6F_9$ at different concentrations. (A) $F_9N_6F_9$ (0.002 wt.% below CAC), (B) $F_9N_6F_9$ (0.005 wt.% below CAC), (C) $F_9N_6F_9$ (0.02 wt.% above CAC), and (D) $F_9N_6F_9$ (0.05 wt.% above CAC) on PAN supports. TMC concentration was maintained at 0.1 wt.% and reaction time was 7 minutes for all membranes.

A

B

C

D

2 µm

1 µm

2 µm

2 µm
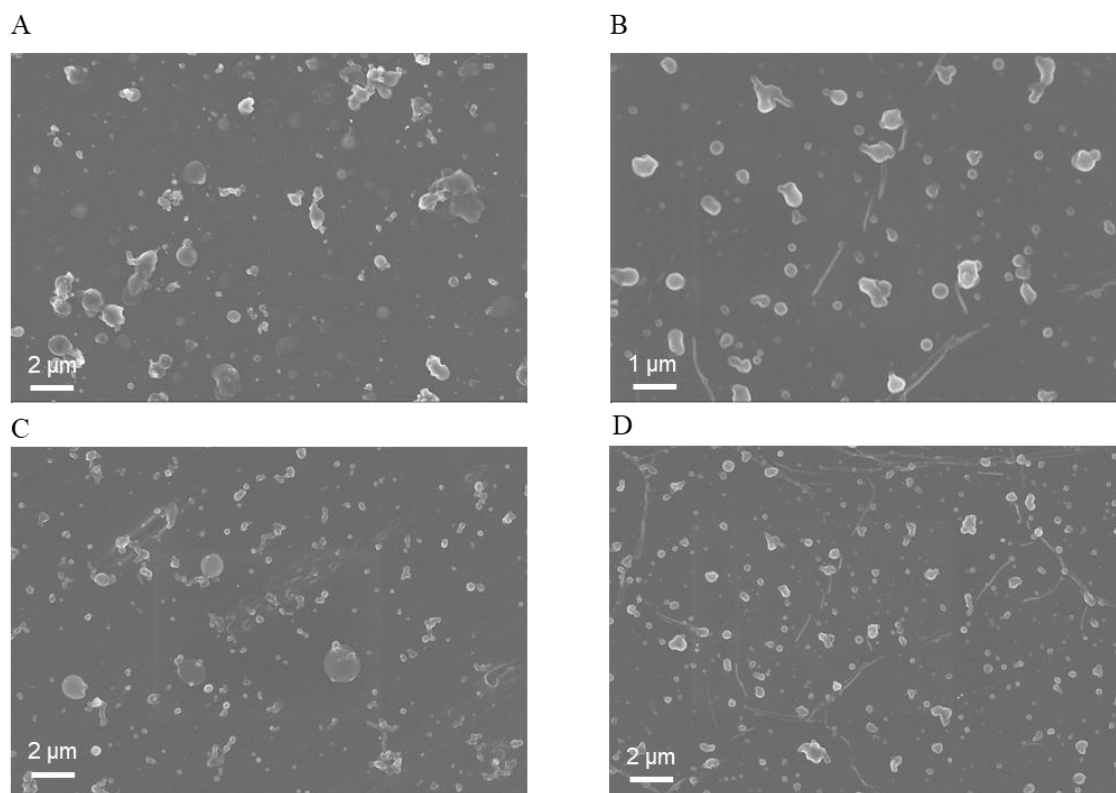
Fig. S18. SEM images of surface morphology of membranes made from (A) $F_{13}N_6F_{13}$ (0.025 wt.%), (B) $C_3N_6C_3$ (0.1 wt.%), (C) $C_6N_6C_6$ (0.1 wt.%), (D) $C_{10}N_6C_{10}$ (0.1 wt.%) and TMC (0.1 wt.%) on PAN supports.

5

A

B

C

D

E

Before activation

F

After activation
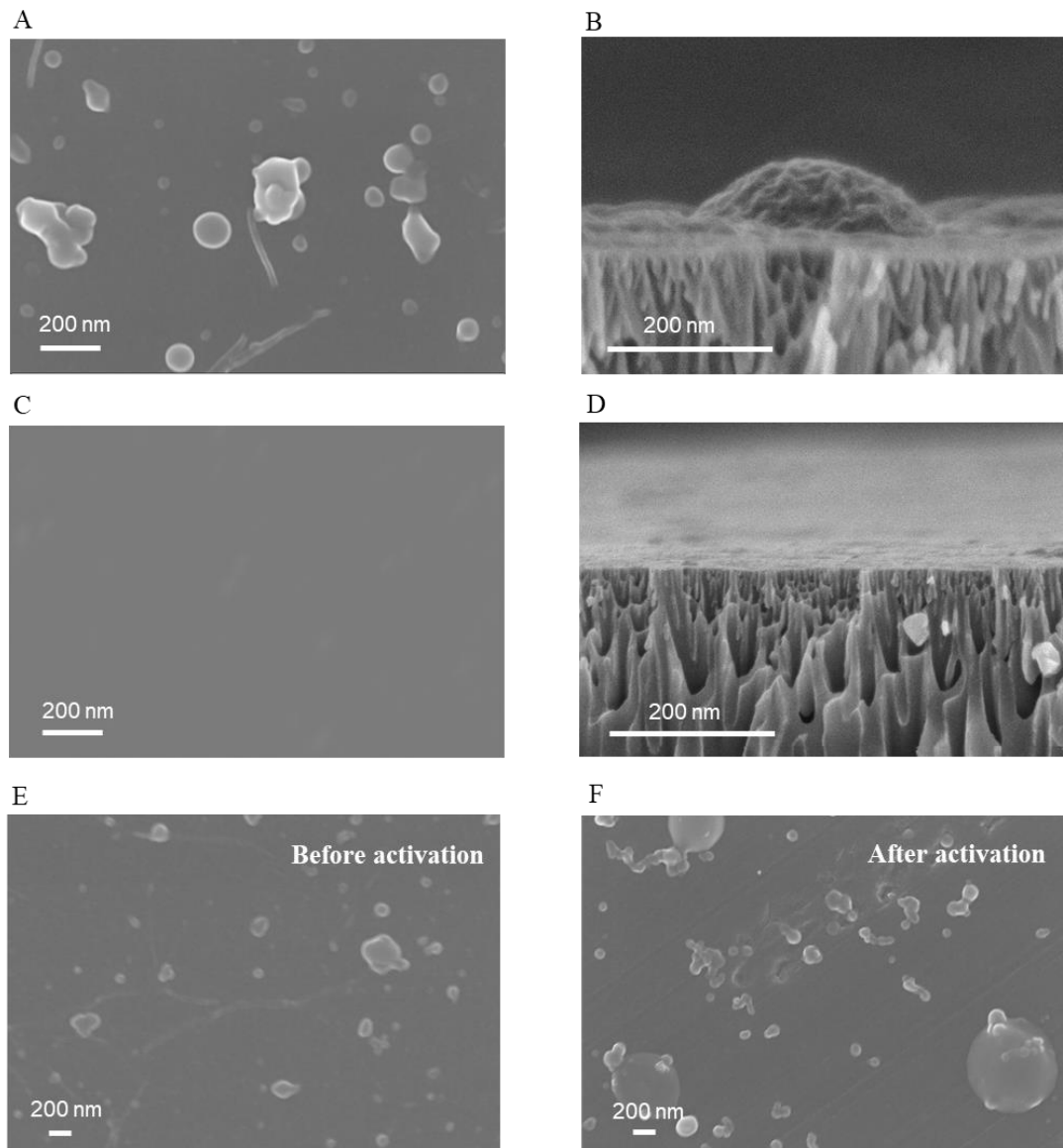
Fig. S19. SEM (A) surface and (B) cross-section images of membranes made using $F_5N_6F_5$ (0.02 wt.%) and TMC (0.1 wt.%) on a PAN support. SEM (C) surface and (D) cross-section images of membranes made by pentaethylenehexamine (N_6) (0.02 wt.%) and TMC (0.1 wt.%) on PAN support. A smooth surface was observed for nanofilms made from N_6 consistent with no formation of vesicles. SEM surface images of membranes made using $F_9N_6F_9$ (0.02 wt.%) and TMC (0.1 wt.%) on PAN support (E) before activation and (F) after activation. There is no obvious change in membrane surface morphology and the circular structures remained after activation.
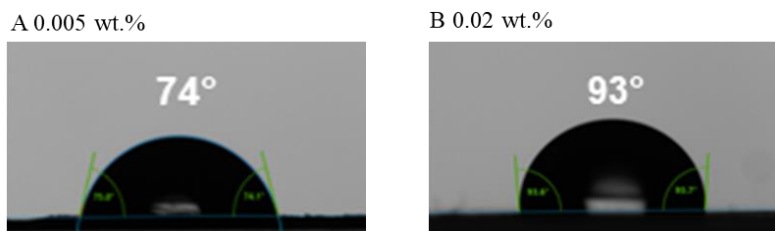
Fig. S20. Water contact angle of (A) membranes made from MOA concentration below CAC (0.005 wt.%). (B) membranes made from MOA concentration above CAC (0.02 wt.%).
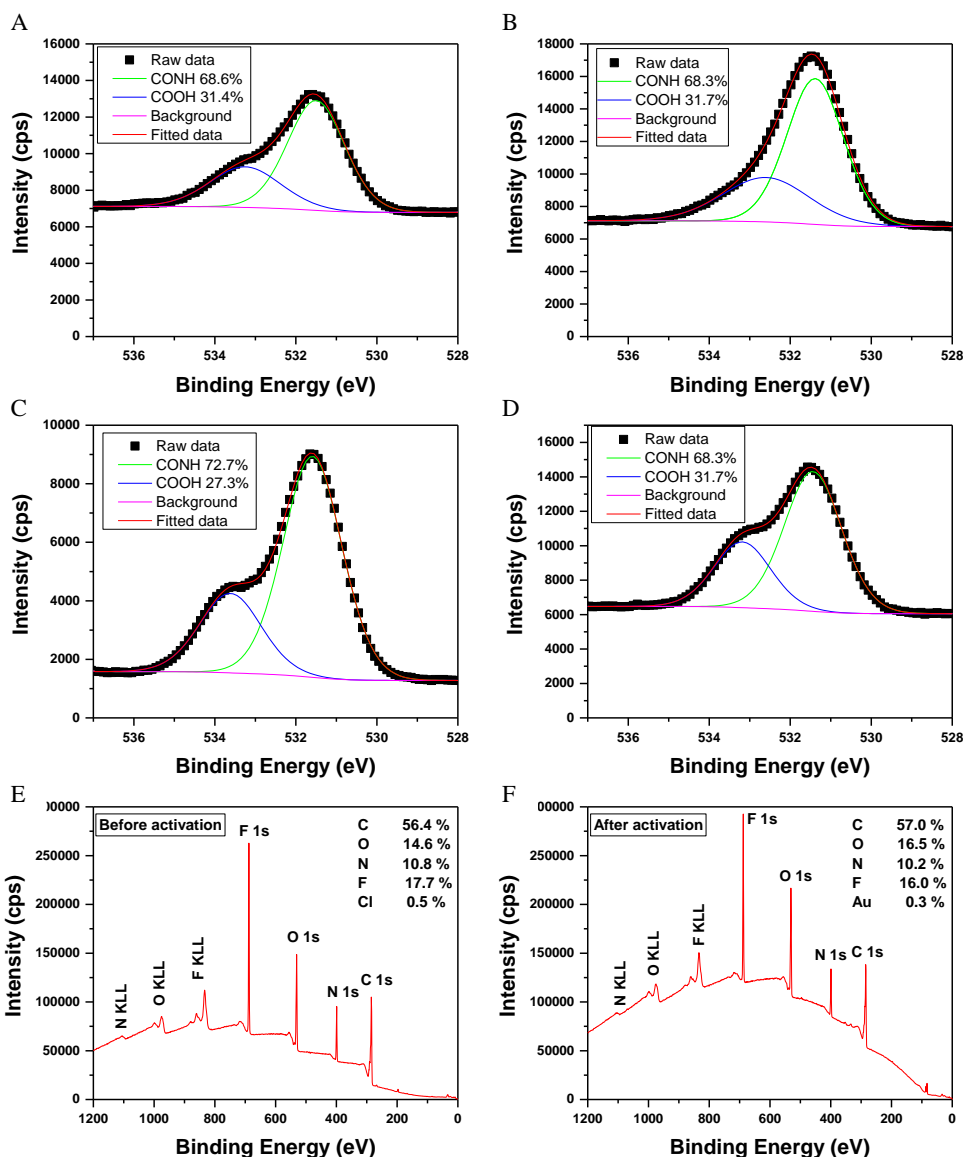
Fig. S21. XPS spectra of free-standing nanofilms transferred to gold coated silicon wafers. O1s narrow scan of (A) $F_5N_6F_5$ (0.005 wt.%) below CAC, (B) $F_5N_6F_5$ (0.02 wt.%) above CAC, (C) $F_5N_6F_5$ (0.2 wt.%) at higher concentration, (D) $C_3N_6C_3$ (0.1 wt.%) nanofilms. Survey scan of $F_9N_6F_9$ (0.05 wt.%) nanofilms (E) before activation, and (F) after activation. No obvious change in chemical composition was found after solvent activation.
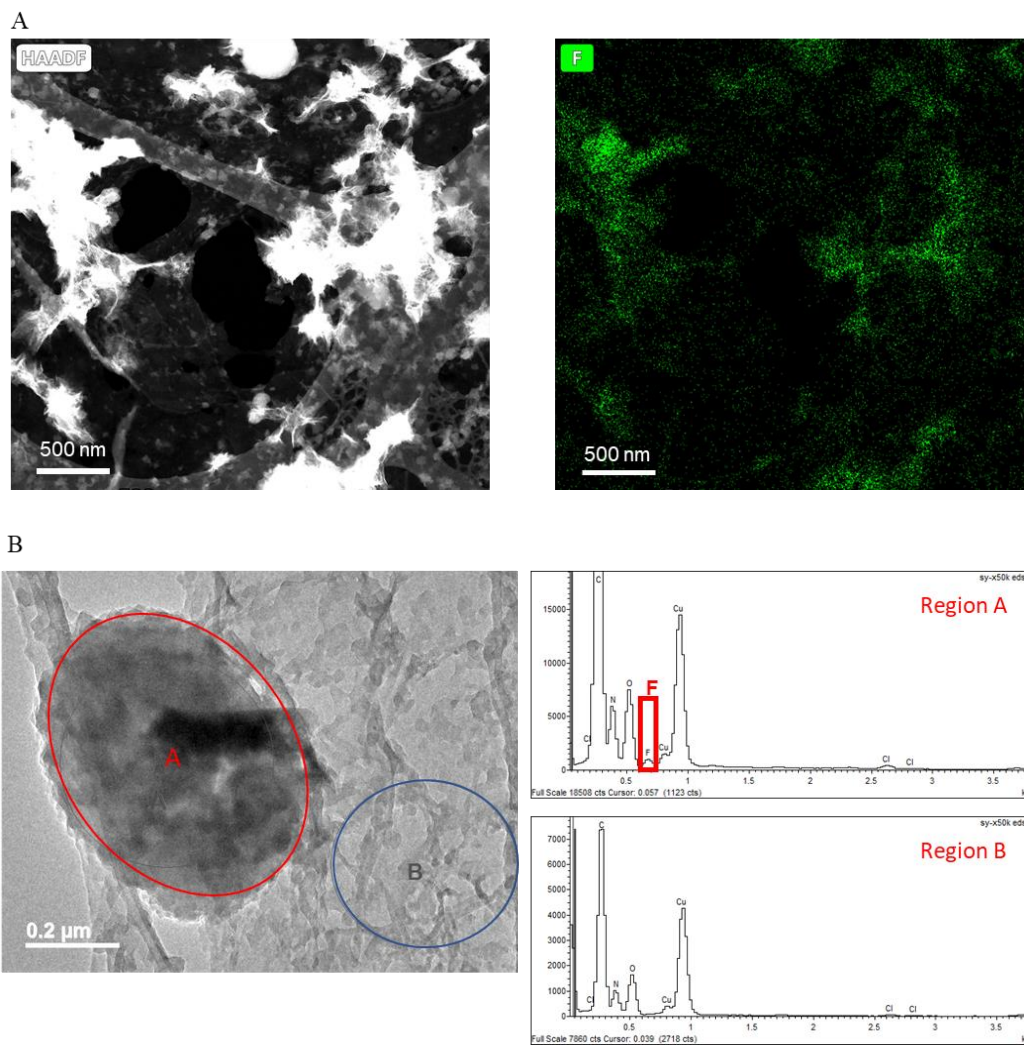
5

Fig. S22. (A) HAADF-STEM images and fluorine mapping for nanofilms made from $F_9N_6F_9$ (0.05 wt.%) and TMC (0.1 wt.%). The intense green aggregates indicate vesicles formed by self-assembly of $F_9N_6F_9$ which are richer in fluorine compared to the surrounding polymer network. The shapes of aggregates are irregular, which could be attributed to the aggregation of vesicles at high concentrations. (B) TEM images and EDX fluorine mapping for membrane made from $F_9N_6F_9$ (0.1 wt.%) and TMC (0.1 wt.%).

15
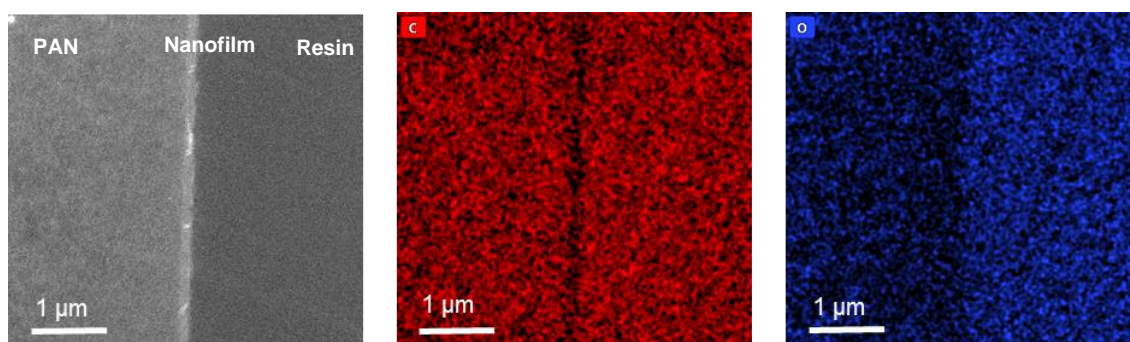
Fig. S23. HAADF-STEM images and element mapping (Carbon in red and Oxygen in blue) for membrane made from $F_5N_6F_5$ (0.1 wt.%) and TMC (0.1 wt.%).
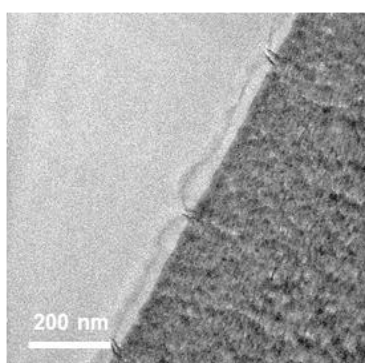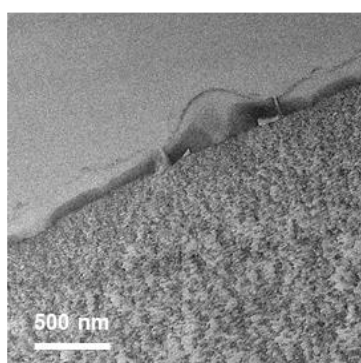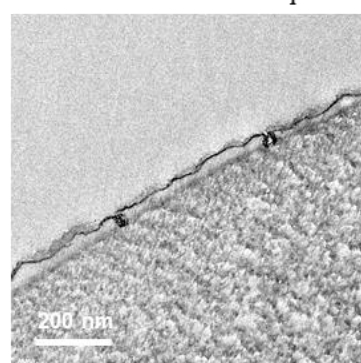
Fig. S24. TEM cross-section images for membranes made from (A) $F_5N_6F_5$ 0.1 wt.% and (B) $F_5N_6F_5$ 0.2 wt.% and TMC (0.1 wt.%) before being pressurized. The successful incorporation of hollow vesicles was observed. (C) TEM cross-section images for membranes made from $F_5N_6F_5$ after being pressurized under 10 bar. The vesicle structures remain after pressurization.
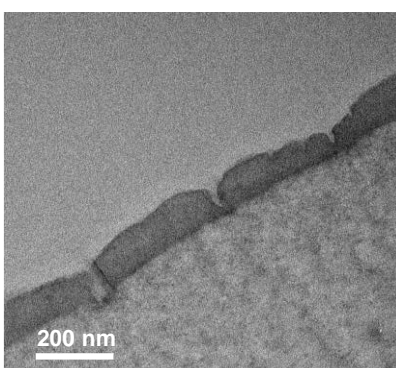
Fig. S25. TEM cross-section images for membranes made from $C_6N_6C_6$ (0.1 wt.%) after being pressurized under 10 bar. The vesicle structures remain after pressurization.
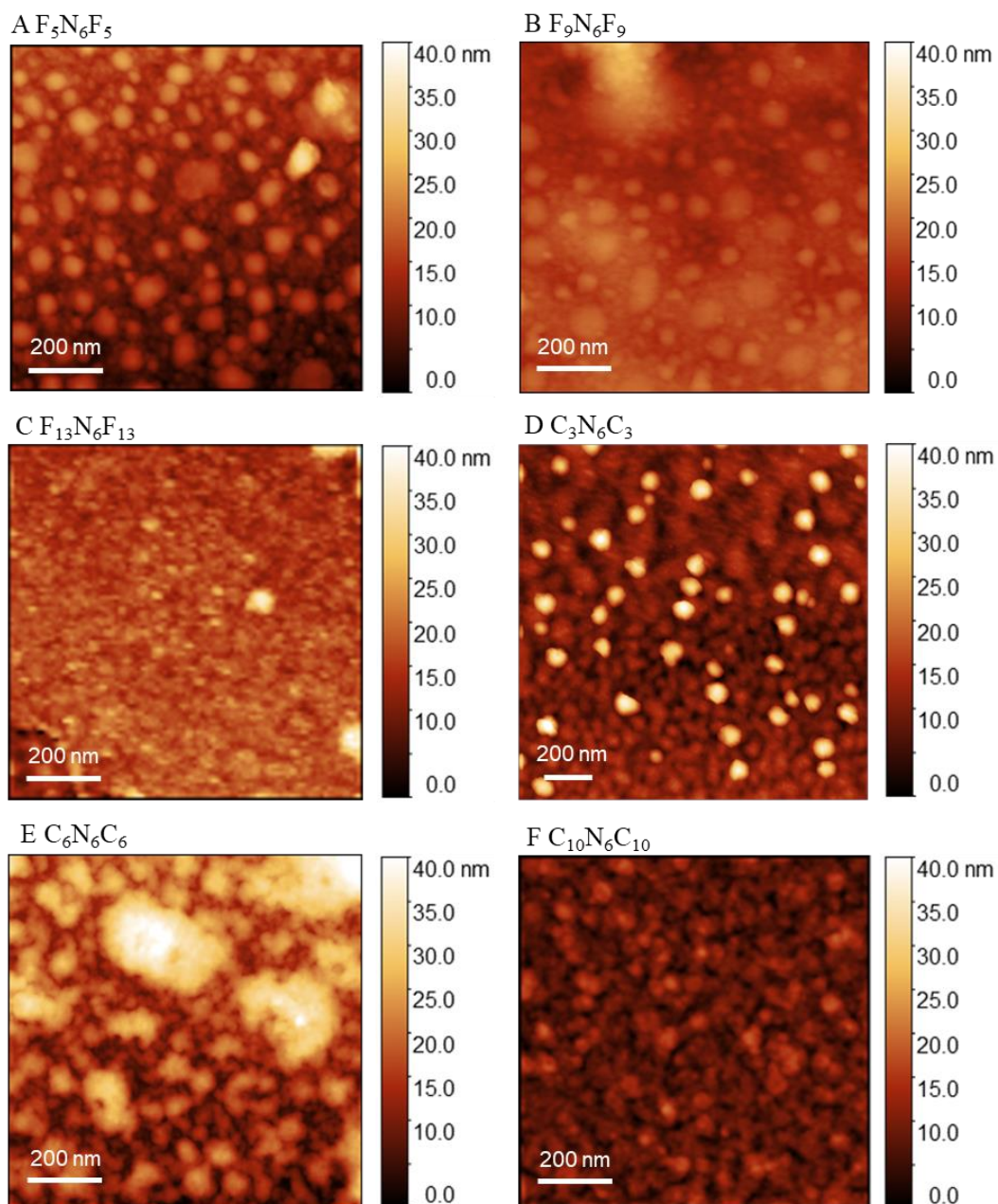
Fig. S26. AFM surface morphology for nanofilms made from (A) $F_5N_6F_5$ (0.02 wt.%), (B) $F_9N_6F_9$ (0.02 wt.%), (C) $F_{13}N_6F_{13}$ (0.025 wt.%), (D) $C_3N_6C_3$ (0.1 wt.%), (E) $C_6N_6C_6$ (0.1 wt.%), (F) $C_{10}N_6C_{10}$ (0.1 wt.%) and TMC (0.1 wt.%) on silicon wafers.

5
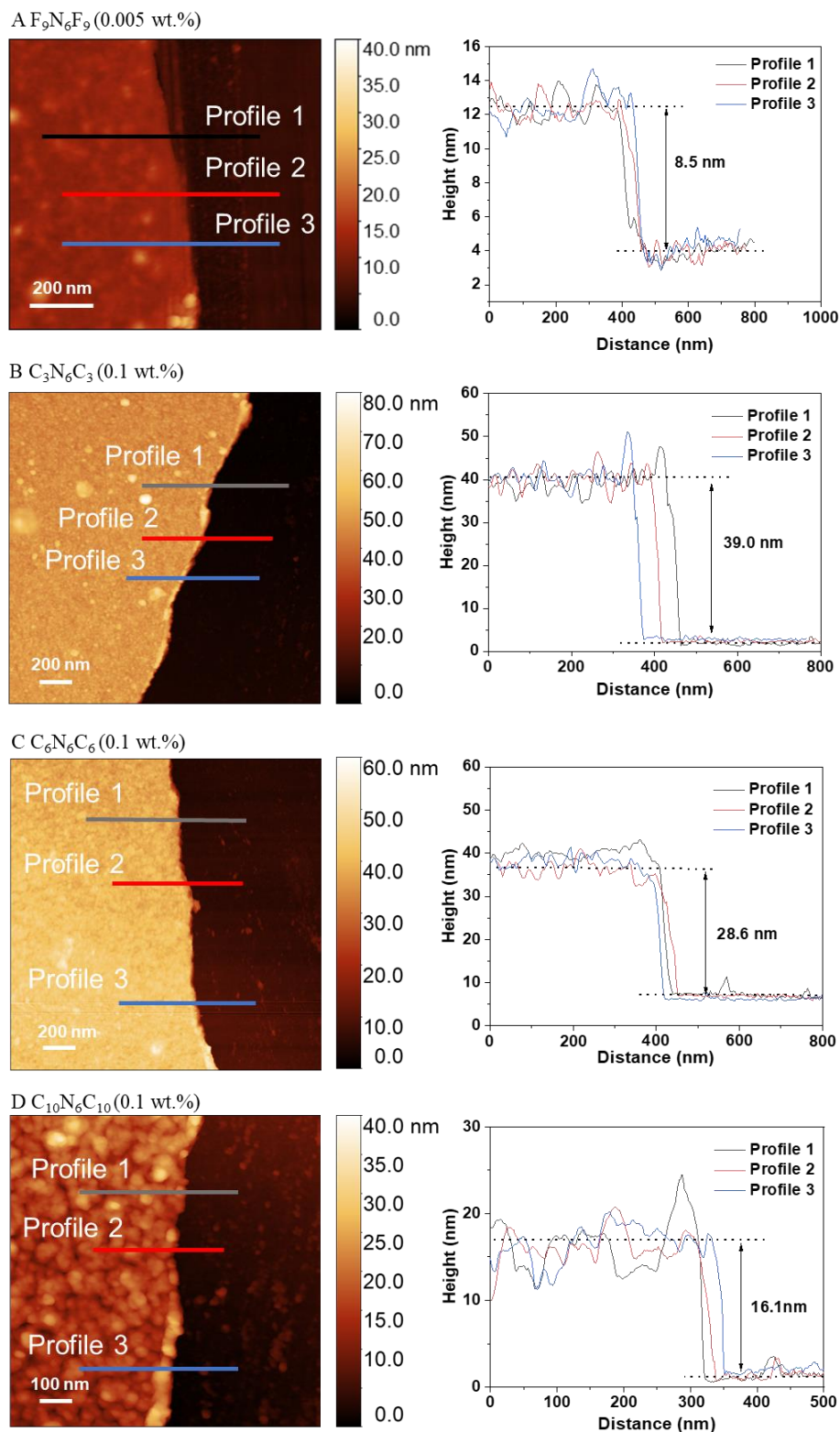
Fig. S27. AFM images and height profiles of membranes made by (A) $F_9N_6F_9$ (0.005 wt.% - below CAC), (B) $C_3N_6C_3$ (0.1 wt.%), (C) $C_6N_6C_6$ (0.1wt.%), and (D) $C_{10}N_6C_{10}$ (0.1 wt.%) and TMC (0.1wt.%) on silicon wafers.

A Before activation
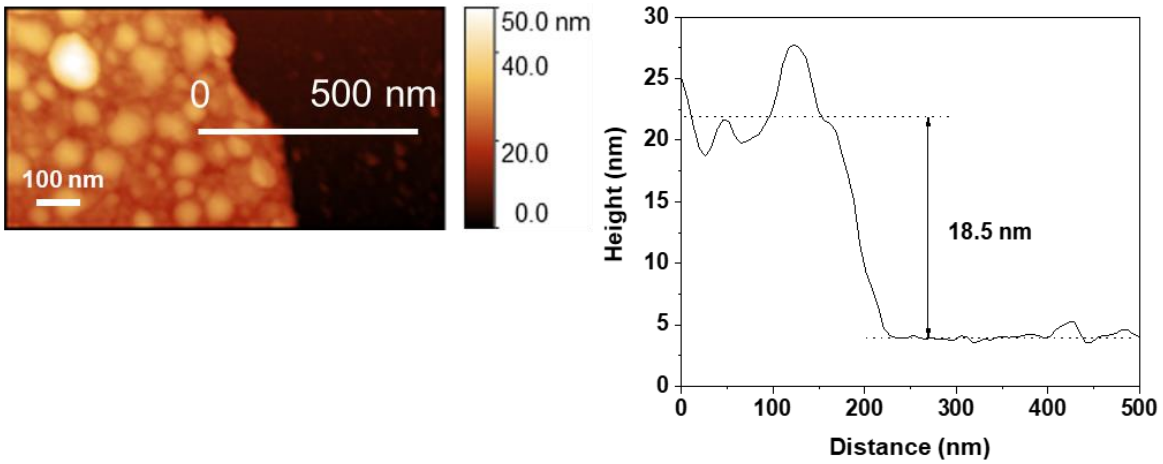
B After activation
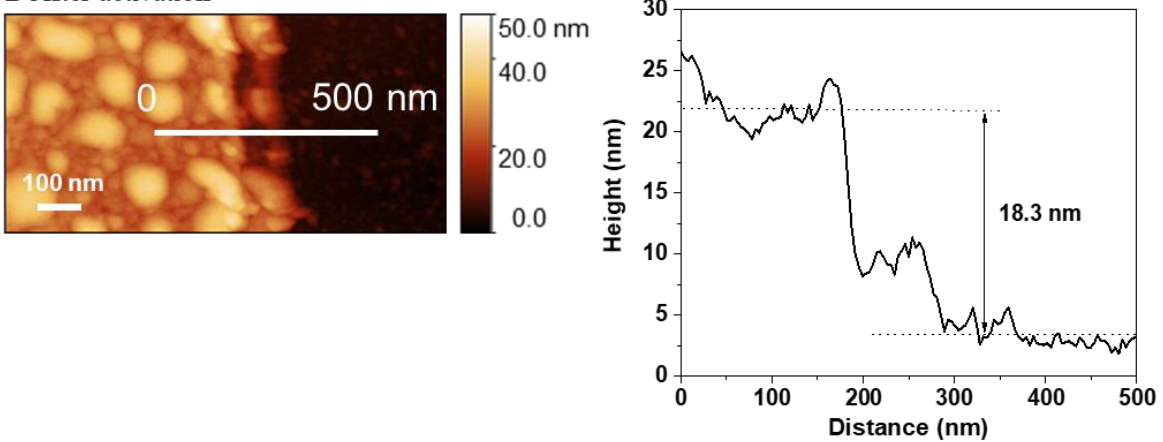
Fig. S28. AFM height images and corresponding height profiles of membranes made from $F_9N_6F_9$ (0.02 wt.%) and TMC (0.1 wt.%) (A) before activation and (B) after activation. Both surface morphology and thickness of nanofilm remain almost the same after activation. We assume the increase of solvent permeance is attributed to molecular level rearrangement of the nanofilms.

3. Nanofiltration performance of MOA membranes
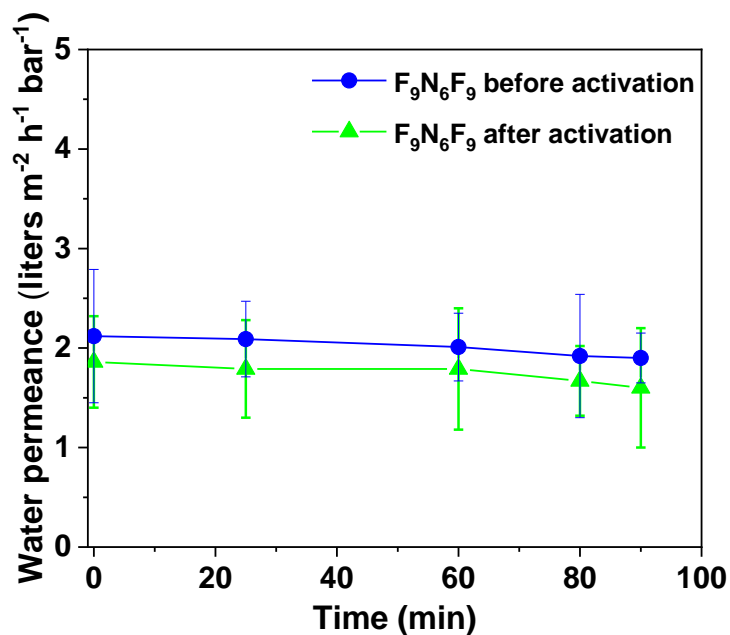
Fig. S29. Water permeance of membranes made from $F_9N_6F_9$ (0.02 wt.%) and TMC (0.1 wt.%) before and after activation. The error bars represent the standard deviation, which was calculated based on the results of three membranes.
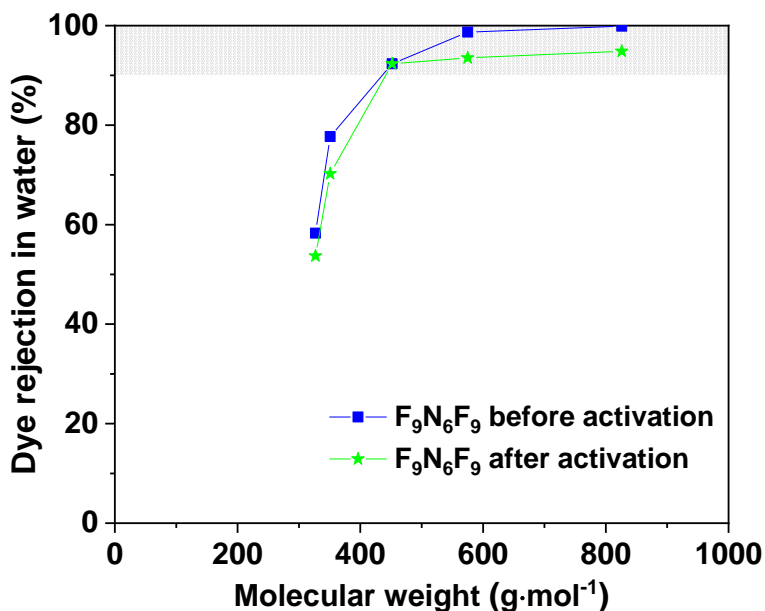
Fig. S30. Dye rejection in water of membranes made from $F_9N_6F_9$ (0.02 wt.%) and TMC (0.1 wt.%) before and after activation. The MWCO for $F_9N_6F_9$ membranes remains the same before

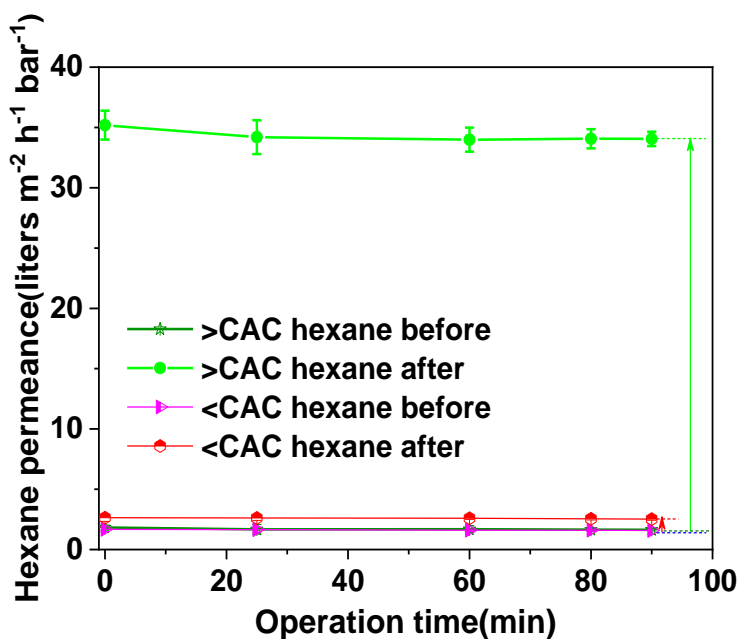and after activation. The error bars represent the standard deviation, which was calculated based on the results of three independent membranes.
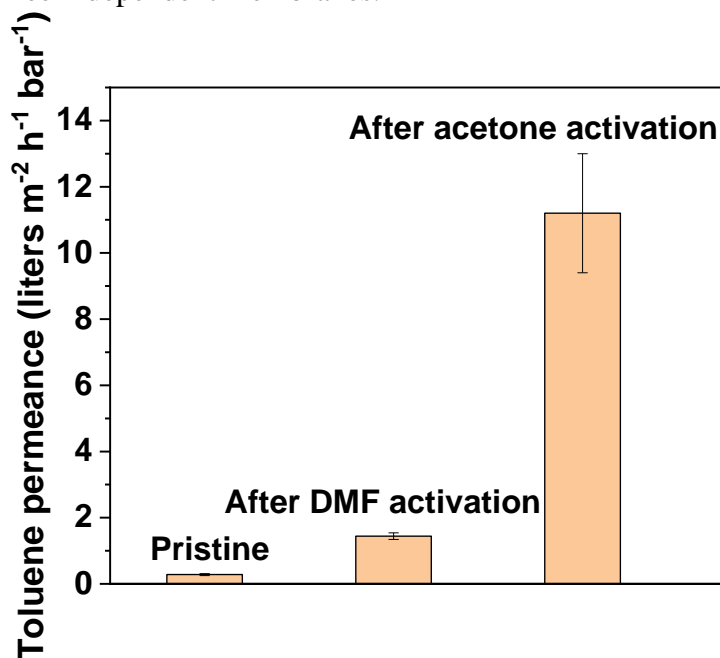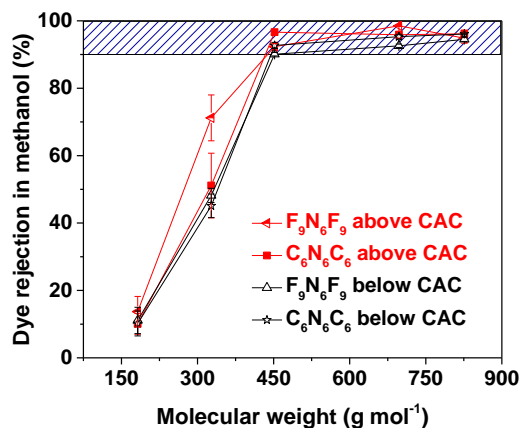

Fig. S31. Comparison of activation impact between DMF and acetone on MOA membranes supported by PEEK. The error bars represent the standard deviation, which was calculated based on the results of three membranes.
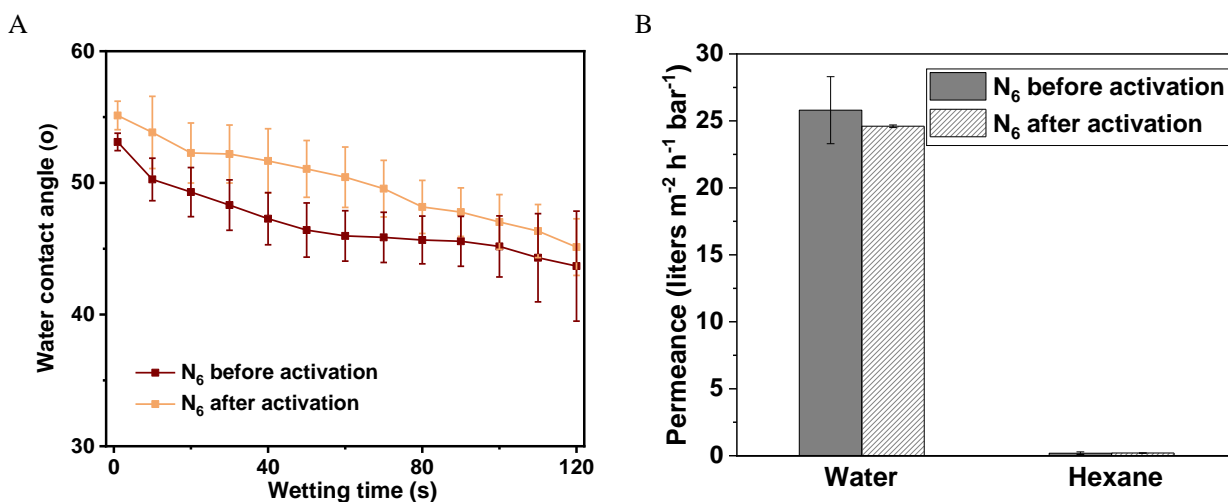
Fig. S32. (A) Water contact angle of pentaethylenehexamine (N_6) (0.02 wt.%) membrane before and after activation. No obvious change is found. **(B)** Hexane and water permeance of membranes made from pentaethylenehexamine (N_6) (0.02 wt.%) and TMC (0.1 wt.%) before and after

activation. The error bars represent the standard deviation, which was calculated based on the results of three samples.

Table S1. Properties of solvents used for organic solvent nanofiltration.

Solvent	Solubility parameter, δ, (MPa$^{0.5}$)	Viscosity, μ, (10^{-3} Pa.s)	Polarity index
Water	48.0	0.89	9.0
Methanol	29.7	0.49	5.1
Hexane	14.4	0.297	0.1
Heptane	15.3	0.33	0.1
Toluene	18.2	0.52	2.4
Acetone	20.1	0.29	5.1
Dimethylformamide	24.8	0.77	6.4

5
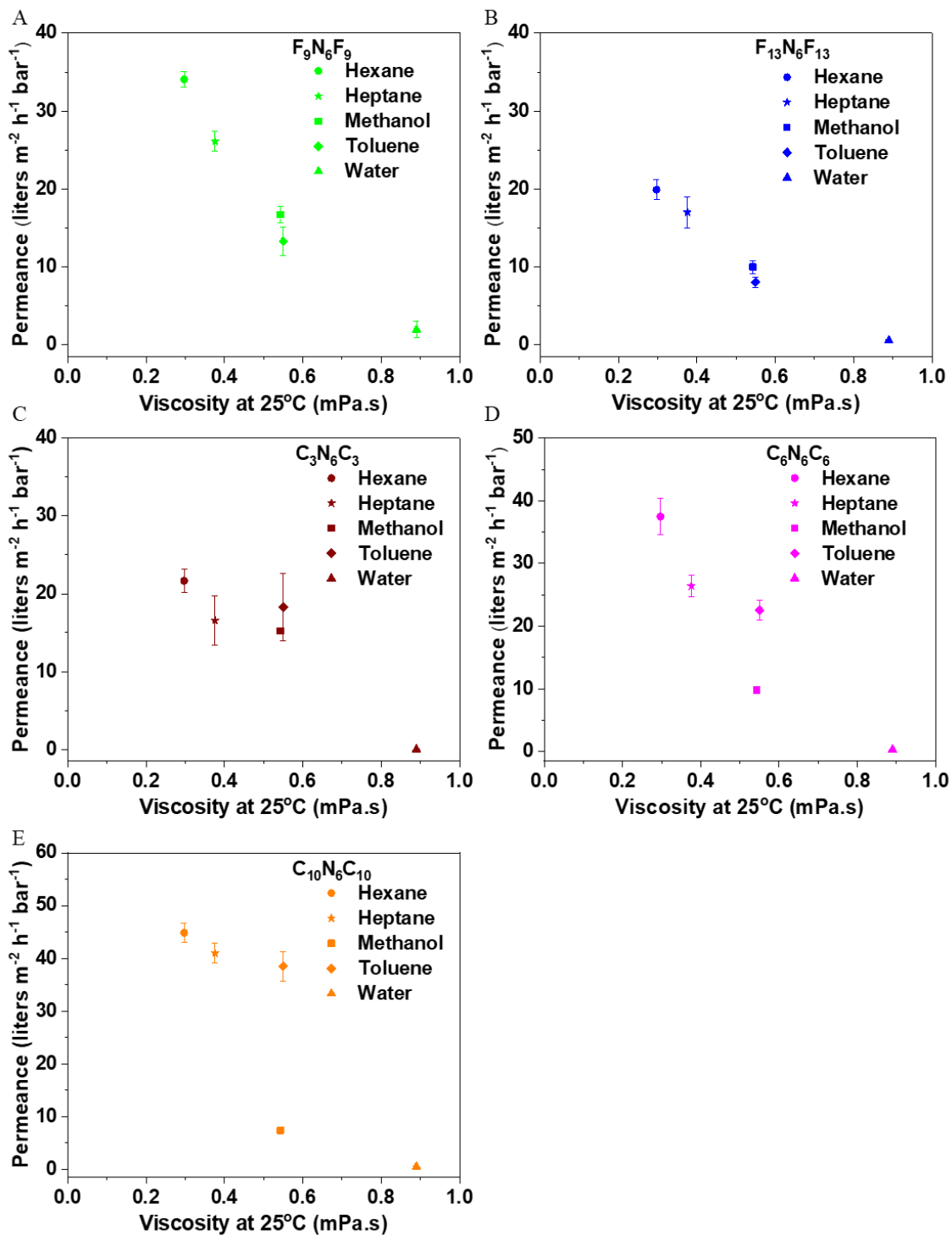
Fig. S33. Solvent permeance of membranes made from (A) $F_9N_6F_9$ (0.02 wt.%-0.1 wt.%-7min), (B) $F_{13}N_6F_{13}$ (0.025 wt.%- 0.1 wt.%-7min), (C) $C_3N_6C_3$ (0.1 wt.%- 0.1 wt.%-1min), (D) $C_6N_6C_6$ (0.1 wt.%-0.1 wt.%-3min), and (E) $C_{10}N_6C_{10}$ (0.1 wt.%-0.1 wt.%-7min) on PAN supports. The membrane fabrication conditions are written as MOA concentration-TMC concentration-Reaction

5

time. The error bars represent the standard deviation, which was calculated based on the results of three independent membranes.
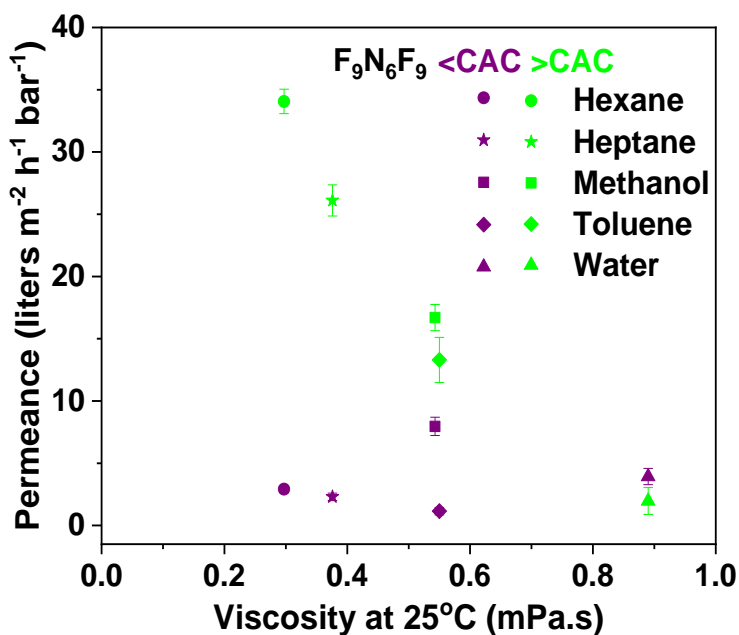

**Fig. S34.** Solvent permeance of $F_9N_6F_9$ membranes with concentration 0.005 wt.% (below CAC) and 0.02 wt.% (above CAC). The error bars represent the standard deviation, which was calculated based on the results of three membranes.

Fig. S35. Hexane permeance of $F_9N_6F_9$ membranes with concentration 0.005 wt.% (below CAC) and 0.02 wt.% (above CAC) before and after activation. Membranes made with MOA

concentration above CAC exhibited significant increase for hexane, while the ones made with MOA concentration below CAC had negligible hexane increase. The error bars represent the standard deviation, which was calculated based on the results of three membranes.

Fig. S36. Rejection of MOA membranes below and above CAC ($F_9N_6F_9$ and $C_6N_6C_6$) versus the molecular weight of dyes in methanol at 10 bar. The error bars represent the standard deviation, which was calculated based on the results of three independent membranes.
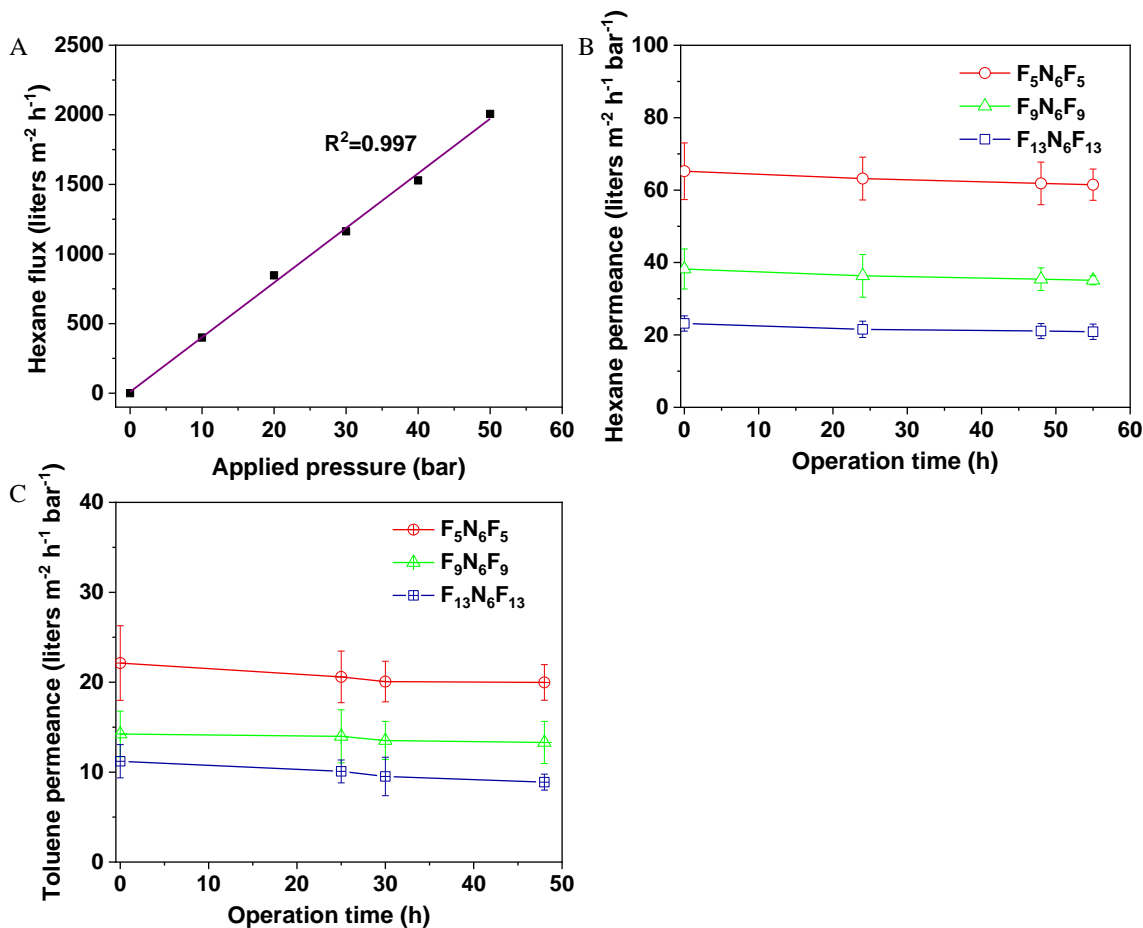
Fig. S37. (A) Variation of hexane flux under varying pressure demonstrating the robustness of the vesicles incorporated into $F_9N_6F_9$ nanofilms ($F_9N_6F_9$-0.02%-7min) on PAN supports. Plot of (B) hexane and (C) toluene permeance with time for $F_5N_6F_5$, $F_9N_6F_9$ and $F_{13}N_6F_{13}$ membranes (10 bar, crossflow rig). The error bars represent the standard deviation, which was calculated based on the results of three independent membranes.
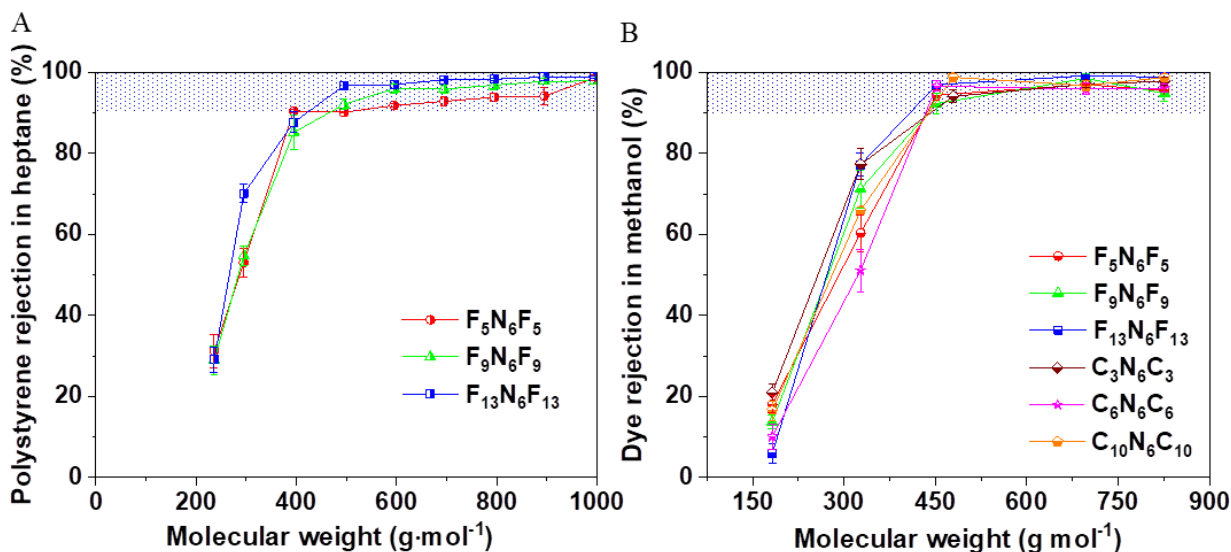
Fig. S38. (A) Rejection of MOA membranes ($F_5N_6F_5$, $F_9N_6F_9$ and $F_{13}N_6F_{13}$) versus the molecular weight of polystyrene oligomers and dimer in heptane. The styrene oligomer mix contained 1 g L^{-1} each of PS 580 and PS 1100 (Agilent) along with 0.1 g L^{-1} of α-methylstyrene dimer. (B) Rejection of MOA membranes ($F_5N_6F_5$, $F_9N_6F_9$, $F_{13}N_6F_{13}$, $C_3N_6C_3$, $C_6N_6C_6$ and $C_{10}N_6C_{10}$) versus the molecular weight of dyes in methanol at 10 bar. The dye concentration is 20 ppm. The error bars represent the standard deviation, which was calculated based on the results of three independent membranes.
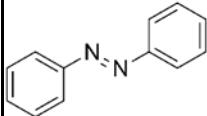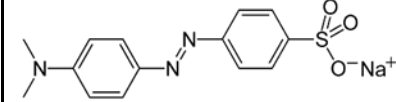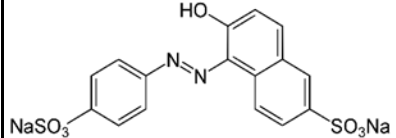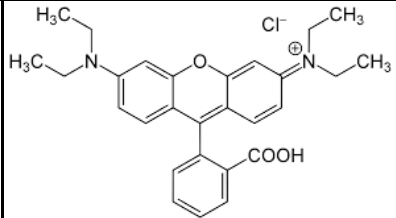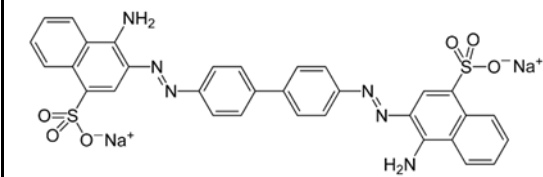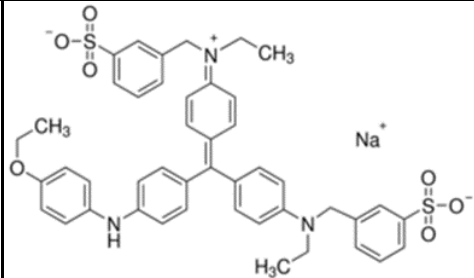
5

Table S2. Properties of dye molecules used for OSN. Charge 0 denotes neutral charge, and - denotes negative charge**.**

Dye molecule name	Molecular weight (g mol⁻¹)	Charge	Structure
Azobenzene (AZB)	182	0	
Methyl orange (MO)	327	-	
Sunset yellow (SY)	452	-	
Rhodamine B dye (RB)	479	+	
Congo red (CR)	696	-	
Brilliant blue R (BB)	826	-	

10
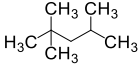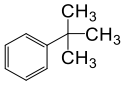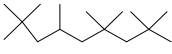
5

Table S3. Comparison of heptane permeance and MWCO between membranes reported in literature and membranes fabricated from MOAs in this work.

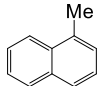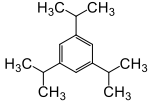| Membrane material	Heptane permeance (liters m^{-2} hour^{-1} bar^{-1})	MWCO (g mol^{-1})	Ref
Priamine-TA	2.5	235	(12)
PIM-1	16.4	535	(23)
PIM-1	4.2	240	(24)
PIM-1	5.5	795	(25)
Epoxysilicones	6.0	650	(26)
PuraMem 600S	1.0	595	Tested in this work
ONf-2	6.0	695	Tested in this work
F$_5$N$_6$F$_5$	47.6	395	This work
F$_9$N$_6$F$_9$	25.4	450	This work
F$_{13}$N$_6$F$_{13}$	17.5	420	This work
C$_3$N$_6$C$_3$	18.1	395	This work
C$_6$N$_6$C$_6$	24.1	395	This work
C$_{10}$N$_6$C$_{10}$	39.0	395	This work

4. Hydrocarbon separation performance

Table S4. Feed composition of synthetic crude oil.

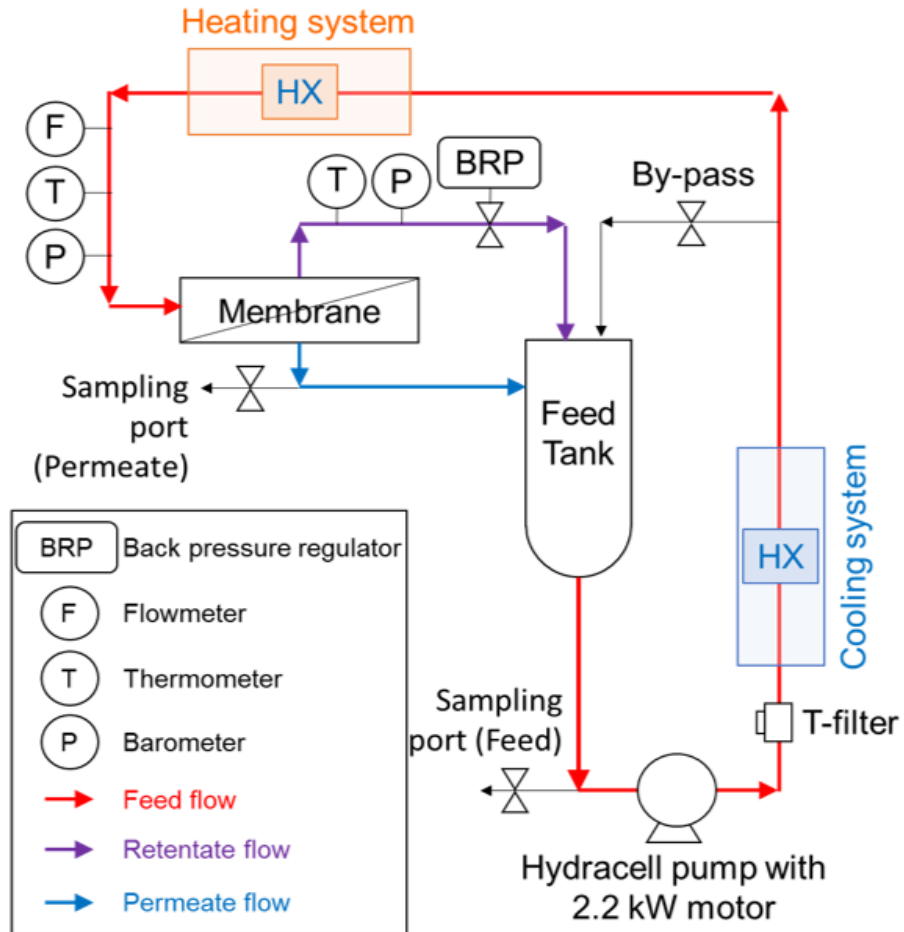| Composition	Structure	MW (g.mol⁻¹)	Feed Concentration(mol%)
Toluene		92.1	17
Methylcyclohexane		98.2	28
n-Octane	n-C$_8$H$_{18}$	114.2	22
iso-Octane		114.2	15
Ter-butylbenzene		134.2	2.2
Decalin		138.3	11
1-Methylnaphthanlene		142.2	2
1,3,5-Triisopropylbenzene		204.4	1.6
iso-Cetane		226.5	1.3

Fig. S39. Schematic of crossflow synthetic crude oil testing system.

5
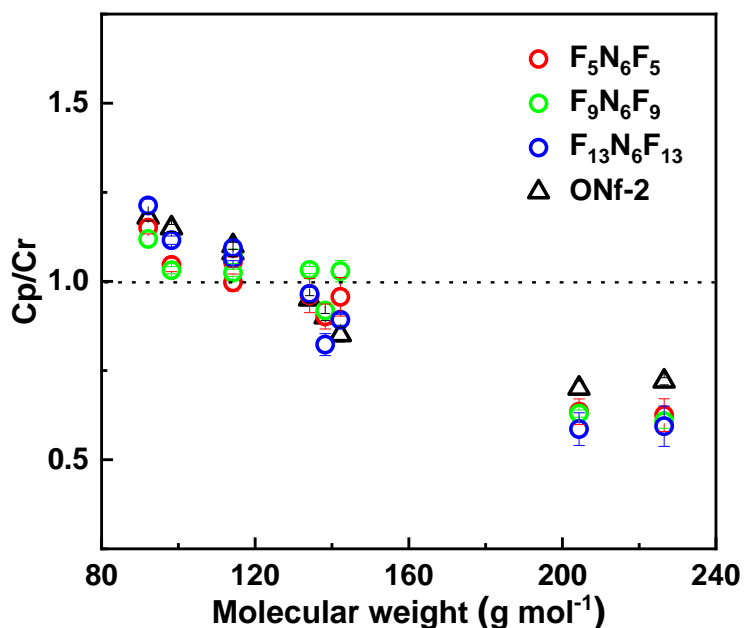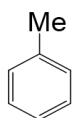
Fig. S40. Ratio of concentrations in permeate (Cp) versus retentate (Cr) of components in a complex mixture, model crude oil fractionated by $F_5N_6F_5$, $F_9N_6F_9$, $F_{13}N_6F_{13}$ and commercial ONf-2 membranes (40 bar, 22 °C, crossflow rig). The error bars represent the standard deviation, which was calculated based on the results of three independent membranes.

Table S5. Separation factors for $C_3N_6C_3$ membrane, literature-reported SBAD-1 membrane and commercial ONf-2 membrane tested in this work.

Separation factor		$C_3N_6C_3$	SBAD-1 (5)	ONf-2
Me ... VS. ...		3.8	2.3	1.6
n-C_8H_{18} VS. ...		4.1	3.2	1.5
Me ... VS. ...		1.5	1.4	0.9

Fig. S41. Ratio of concentrations in permeate (Cp) versus retentate (Cr) of components in a complex mixture, model crude oil fractionated by $C_3N_6C_3$ membrane and ONf-2 membrane at 50 °C. MOA membrane remained good separation performance and exhibited excellent thermal stability.
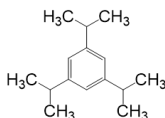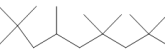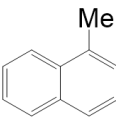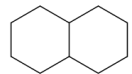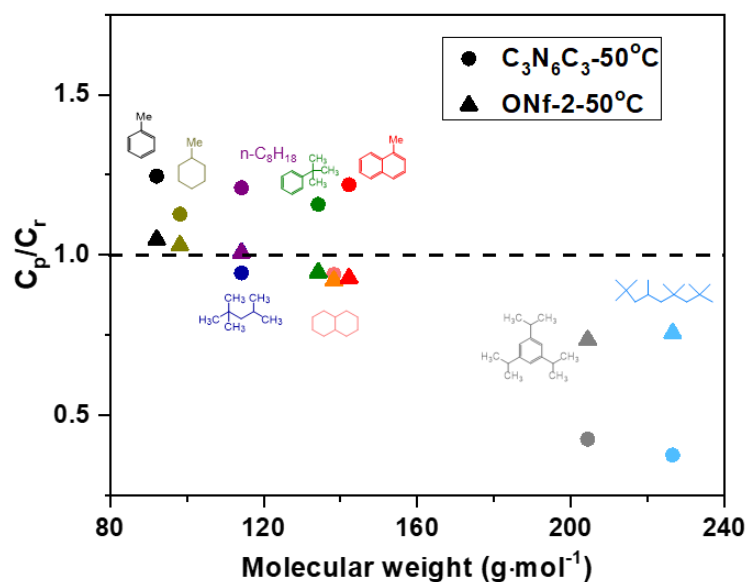
Table S6. Summary of separation performance of synthetic crude oil (Cp/Cr) of MOA membranes, SBAD-1 membrane and commercially available membranes.

Membrane	Permeance (liters m^{-2} h^{-1} bar^{-1})	Selectivity (Concentration of permeate per concentration of retentate, Cp/Cr)								
		1 (92.1)	2 (98.2)	3 (114.2)	4 (114.2)	5 (134.2)	6 (138.3)	7 (142.2)	8 (204.4)	9 (226.5)
		Toluene	Methyl Cyclohexane	n-Octane	iso-Octane	TBB	Decalin	1-Methyl Naphthalene	TIB	iso-Cetane
F$_5$N$_6$F$_5$	4.2 ± 0.4	1.16 ± 0.02	1.05 ± 0.02	1.05 ± 0.01	1.00 ± 0.02	0.94 ± 0.05	0.91 ± 0.04	0.95 ± 0.05	0.63 ± 0.04	0.62 ± 0.05
F$_9$N$_6$F$_9$	2.9 ± 0.4	1.12 ± 0.03	1.04 ± 0.02	1.08 ± 0.02	1.03 ± 0.02	1.04 ± 0.03	0.92 ± 0.02	1.03 ± 0.03	0.63 ± 0.01	0.60 ± 0.02
F$_{13}$N$_6$F$_{13}$	0.9 ± 0.2	1.21 ± 0.02	1.12 ± 0.01	1.06 ± 0.02	1.09 ± 0.02	0.97 ± 0.02	0.83 ± 0.03	0.90 ± 0.01	0.59 ± 0.04	0.59 ± 0.05
C$_3$N$_6$C$_3$	0.1 ± 0.2	1.21 ± 0.02	1.01 ± 0.02	1.20 ± 0.03	0.83 ± 0.01	1.11 ± 0.03	0.92 ± 0.01	1.29 ± 0.06	0.46 ± 0.06	0.30 ± 0.01
C$_6$N$_6$C$_6$	1.1 ± 0.2	1.18 ± 0.04	1.06 ± 0.03	1.10 ± 0.04	0.97 ± 0.02	1.07 ± 0.03	0.95 ± 0.04	1.17 ± 0.05	0.52 ± 0.04	0.43 ± 0.05
C$_6$N$_6$C$_6$ in-situ	5.3 ± 1.2	1.09 ± 0.01	1.02 ± 0.00	1.06 ± 0.01	0.96 ± 0.01	1.03 ± 0.01	0.97 ± 0.01	1.06 ± 0.02	0.76 ± 0.02	0.72 ± 0.01
C$_{10}$N$_6$C$_{10}$	8.4 ± 0.1	1.05 ± 0.02	1.04 ± 0.01	1.10 ± 0.02	1.01 ± 0.01	0.99 ± 0.01	0.99 ± 0.01	1.11 ± 0.03	0.77 ± 0.02	0.72 ± 0.03
Borsig/GMT-ONf-2	3.0 ± 0.2	1.18 ± 0.01	1.15 ± 0.01	1.10 ± 0.01	1.08 ± 0.01	0.95 ± 0.01	0.90 ± 0.01	0.85 ± 0.02	0.70 ± 0.02	0.72 ± 0.01
SBAD-1	0.022	1.18 ± 0.02	0.90 ± 0.01	1.11 ± 0.02	0.82 ± 0.05	1.25 ± 0.03	1.03 ± 0.00	1.40 ± 0.05	0.52 ± 0.07	0.34 ±0.06
PuraMem® Flux	1.13 ± 0.04	1.01 ± 0.00	1.06 ± 0.00	1.11 ± 0.00	1.05 ± 0.00	0.95 ± 0.01	0.89 ± 0.01	0.91 ± 0.01	0.57 ± 0.02	0.56 ± 0.00
PuraMem® Selective	1.2 ± 0.15	0.99 ± 0.00	1.07 ± 0.00	1.14 ± 0.00	1.07 ± 0.00	0.95 ± 0.01	0.87 ± 0.01	0.95 ± 0.00	0.48 ± 0.00	0.43 ± 0.01
PuraMem® Performance	0.7 ± 0.01	0.98 ± 0.00	1.07 ± 0.00	1.14 ± 0.00	1.08 ± 0.00	0.96 ± 0.04	0.88 ± 0.004	0.97 ± 0.02	0.44 ± 0.02	0.39 ± 0.02
PuraMem® 280	0.1 ± 0.01	0.94 ± 0.03	0.98 ± 0.03	1.11 ± 0.03	1.00 ± 0.03	1.00 ± 0.03	0.95 ± 0.02	1.08 ± 0.04	0.80 ± 0.02	0.80 ± 0.03

A
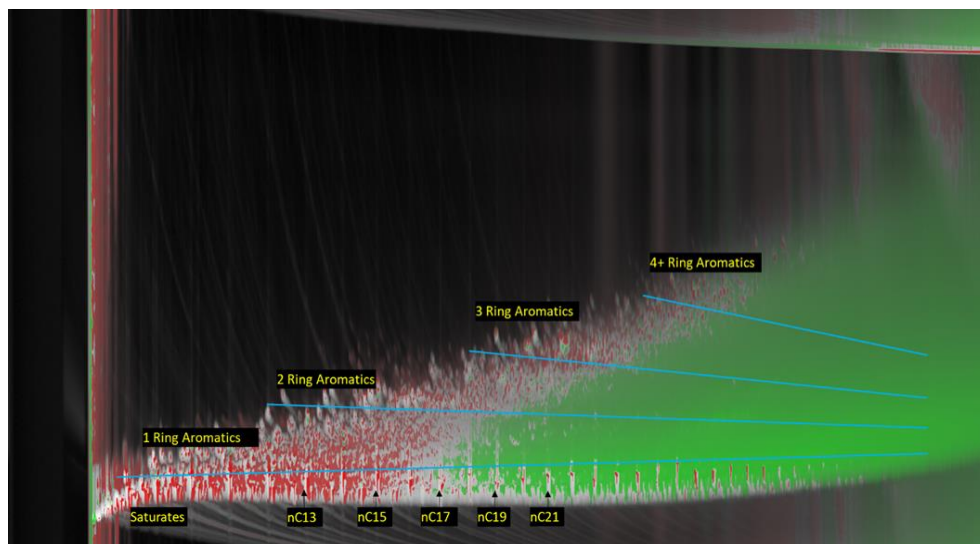
B
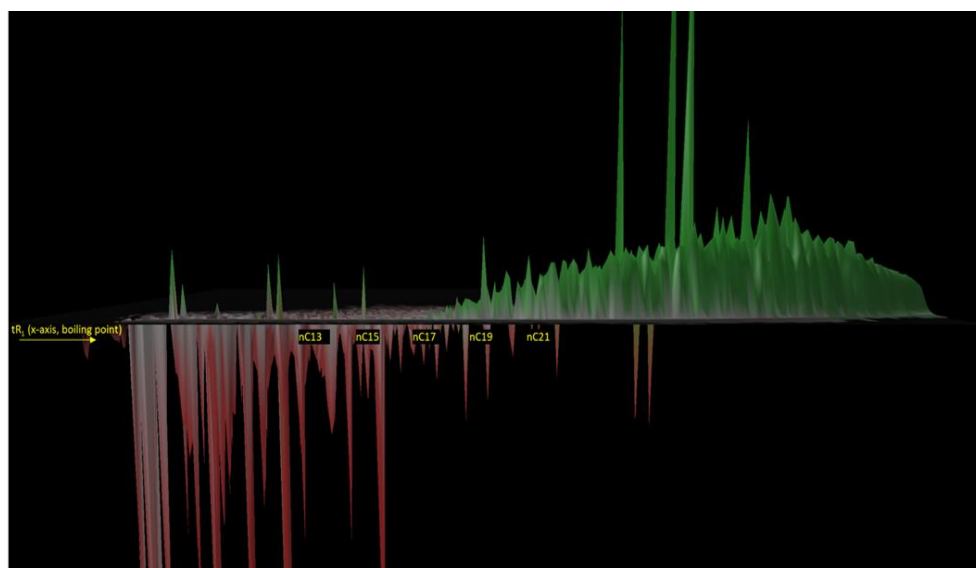
5

Fig. S42. **(A)** GC×GC flame ionization detection (FID) analysis of membrane fractionation of shale-based light crude oil at 22 °C under 43 bar applied pressure. **(B)** Side view of GC×GC-FID [shown in **(A)**] showing the carbon number partition of real crude oil obtained by $F_{13}N_6F_{13}$ membrane. Permeate in red and retentate in green.

10
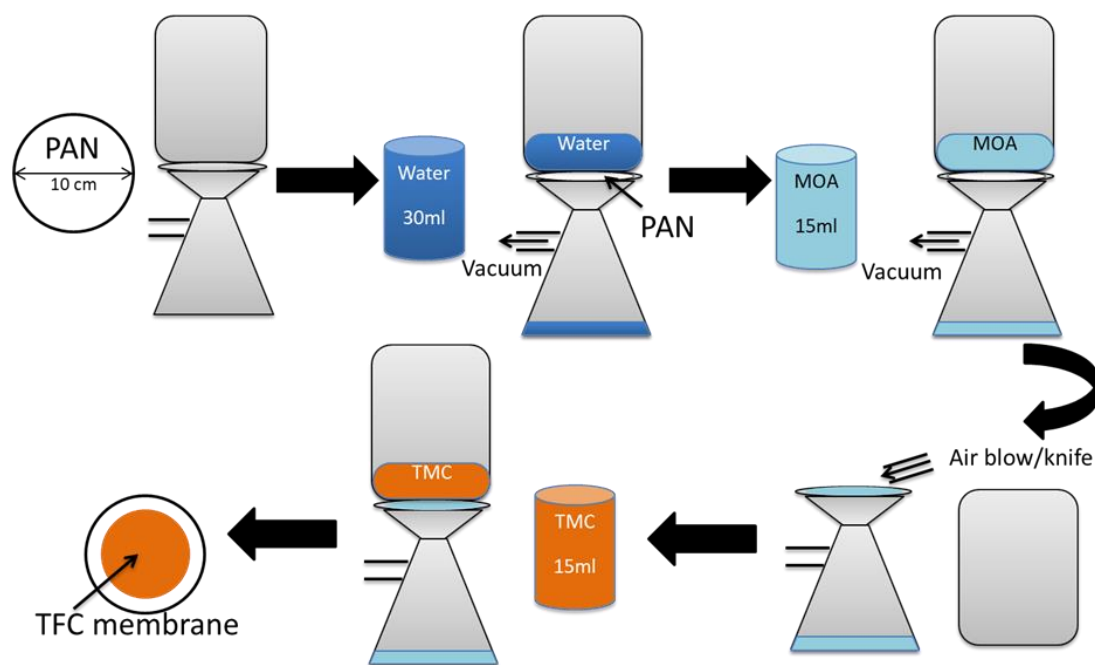
Fig. S43. Schematic illustration of MOA membrane fabrication on an in-situ support. The process starts with the pre-wetting of PAN support with water. The support was then impregnated with concentrated MOA solution where MOA vesicles are enriched. The excess amount of liquid was drained by a vacuum pump until no obvious liquid layer was left on the surface. Air blow was employed to remove the excess aqueous solution from the membrane surface to avoid defect formation during nanofilm formation. Then TMC in n-hexane solution was slowly poured onto the surface for 7 min to initiate the polymerization. After removing the excess organic solution, the resulting membrane was left air-dry for 24 h before characterization and performance testing.
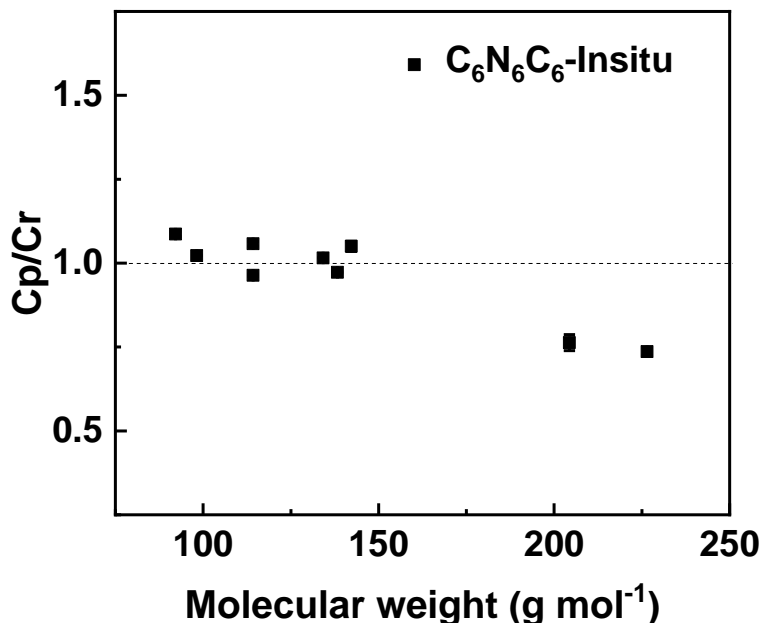
Fig. S44. Ratio of concentrations in permeate (Cp) versus retentate (Cr) of components in a complex mixture, model crude oil fractionated by $C_6N_6C_6$ membranes made by interfacial polymerization on an in-situ PAN support (40 bar, 22 °C, crossflow rig). The error bars represent the standard deviation, which was calculated based on the results of three independent membranes.
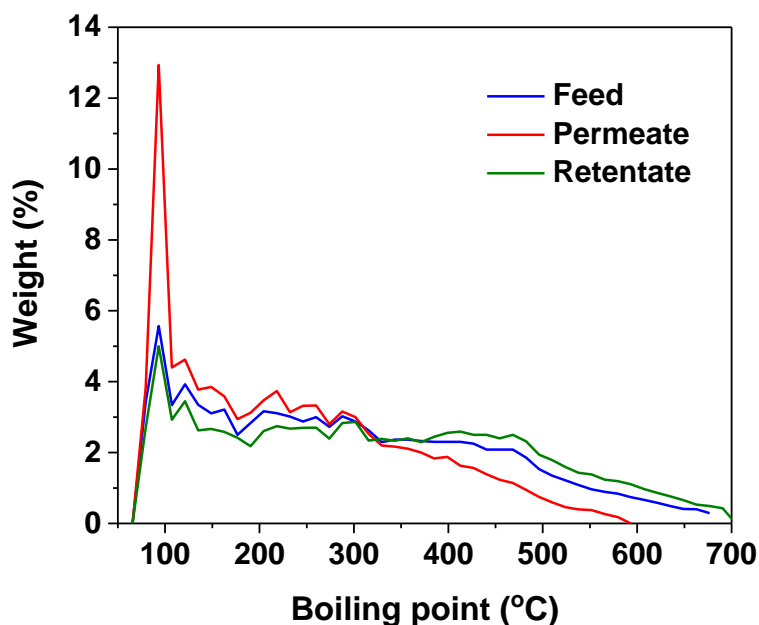
Fig. S45. Boiling-point distribution of feed, permeate, and retentate from $C_6N_6C_6$ membrane fractionation of light shale-based crude oil.

3. Theoretical analysis of light shale crude oil separation data

In this section membrane diffusion theory is applied to the membrane separation of a light shale crude oil. We consider an n component mixture in contact with a planar membrane of thickness ℓ where the fluid diffuses in the positive z dimension. The membrane-retentate interface is located at $z = 0$ and the membrane-permeate interface at $z = \ell$.

The flux N_i for each species i is related to the chemical potential gradient of i through the Onsager relation (*29*),

$$N_i = -L_i \frac{\partial \mu_i}{\partial z} \tag{3}$$

where μ_i is the chemical potential of i within the membrane and L_i is the Onsager coefficient. Note, in Eq. (3) we do not account for coupling of the driving forces.

We define L_i in terms of the mole fraction of **species i, x_i**, molar concentration c, diffusivity D_i, ideal gas constant R and absolute temperature T,

$$L_i = \frac{c}{RT} x_i D_i \tag{4}$$

The mole fraction of the permeate x_i^p is calculated via the flux at the membrane-permeate interface (*28*)

$$x_i^p = \frac{N_i(z=\ell)}{\sum_{j=1}^n N_j(z=\ell)} = \frac{N_i(z=0)}{\sum_{j=1}^n N_j(z=0)} \tag{5}$$

In the second step of Eq. (5) we imposed a restriction to steady state operation. At steady state the flux is constant across the membrane.

Combining Eqns. (3) – (5)

$$x_i^p = \frac{x_{i,0} D_i \left(\frac{d\mu_i}{dz}\right)_{z=0}}{\sum_{j=1}^n x_{j,0} D_j \left(\frac{d\mu_j}{dz}\right)_{z=0}} \tag{6}$$

where $x_{i,0}$ is the mole fraction within the membrane at the retentate boundary. Assuming that the chemical potential exhibits a linear gradient across the membrane we obtain,

$$x_i^p = \frac{x_{i,0} D_i (\mu_i^p - \mu_i^r)}{\sum_{j=1}^n x_{j,0} D_j (\mu_i^p - \mu_i^r)} \tag{7}$$

μ_i^p is the chemical potential in the permeate and μ_i^r is the chemical potential in the retentate. We now define the quantity K_i (Diffusivity and chemical potential)

$$K_i = \frac{x_{i,0}}{x_i^r} D_i \tag{8}$$

x_i^r is the mole fraction of i in the retentate. Combining (7) and (8) we obtain the final result

$$\frac{x_i^p}{x_i^r} = \frac{K_i (\mu_i^p - \mu_i^r)}{\sum_{j=1}^n x_j^r K_j \left(\mu_j^p - \mu_j^r\right)} \tag{9}$$

To use Eq. (9) to predict the membrane-based separation of mixtures one needs to know the solubility and diffusivities of each individual fluid species. This can be achieved through detailed measurements of pure component solubility and flux data within the membrane.

The pure component solubilities can be used to parameterize a mixture thermodynamic model which can be used to predict the solubility in multi-component mixtures (*28, 30*).

In the current class of membranes, we do not have sufficient pure-component diffusion and solubility data to develop such a model for the separation of petroleum mixtures. Instead, we take the pragmatic approach of assuming K_i of a petroleum species i can be expressed as a power law function of its molecular weight, MW_i

$$K_i = aMW_i^{-b} \tag{10}$$

Where a and b are constants which depend on the identity of the membrane. Combining Eqns. (9) and (10)

$$\frac{x_i^p}{x_i^r} = \frac{\mu_i^p - \mu_i^r}{\sum_{j=1}^{n} x_j^r \left(\frac{MW_i}{MW_j}\right)^b \left(\mu_j^p - \mu_j^r\right)} \tag{11}$$

As can be seen, the constant a cancels, and we are left with a 1 parameter model to describe the membrane based separation of crude oil. The larger the value of b, the more effective the membrane is for size based separations.

To characterize petroleum streams, we employ the industry standard methodology of defining petroleum fractions based on boiling point temperature (T_b), specific gravity (*SG*) and molecular weight (*MW*). The petroleum fractions are generated from a simulated distillation curve (SIMDIST, ASTM-D2887) as well as a whole petroleum specific gravity of 0.8 using standard industry methodology (*31*). The crude sample was represented using 40 petroleum fractions which are listed in Table S7.

Table S7. List of 40 petroleum fractions defined by boiling point temperature, molecular weight and specific gravity. Weight percent in a light shale crude is given in the right columns.

$T_b(°C)$	MW	SG	wt%	$T_b(°C)$	MW	SG	wt%
4.8	58.71	0.649	0.627	311.7	249.5	0.834	2.899
21.2	64.48	0.655	0.617	326.9	264.5	0.841	2.785
36.4	70.3	0.665	1.091	342.3	280.3	0.848	2.559
51.7	76.53	0.680	1.820	357.6	296.6	0.855	2.470
66.9	83.03	0.695	2.613	372.9	313.7	0.862	2.372
81.9	89.82	0.705	3.483	388.3	331.5	0.869	2.265
97.3	97.24	0.715	4.301	403.7	350.2	0.876	2.318
111.8	104.5	0.725	4.493	418.9	368.9	0.883	2.231
127.8	113.1	0.734	3.961	440.2	397	0.892	3.659
142.9	121.5	0.744	4.231	467.9	439.9	0.903	3.155
158.4	130.7	0.753	3.664	495.8	490.1	0.914	2.923
173.8	140.2	0.762	3.872	523.3	547.2	0.925	2.388
188.7	149.9	0.770	3.573	551.7	615.2	0.937	2.124
204.4	160.7	0.779	3.422	578.3	683.6	0.953	1.663
219.7	171.7	0.787	3.494	606.1	768.8	0.965	1.137
234.9	183.2	0.795	3.337	633.9	871.9	0.973	0.744
250.3	195.3	0.803	3.300	653.9	959.3	0.977	0.207
265.7	208	0.811	3.289	665.0	1010	0.979	0.172
280.9	221.1	0.819	3.068	677.8	1075	0.982	0.623
296.3	235.1	0.826	2.961	682.8	1095	0.985	0.088

To evaluate Eq. (11) an accurate thermodynamic model to predict the mixture chemical potentials is required. In this work we use the simplified (*32*) polar (*33*) PC-SAFT (*34*) equation of state using the petroleum parameterization methodology of Marshall et al (*35*).

The solution of Eq. (11) assumes a constant temperature, pressure and composition on the retentate side of the membrane. The permeate mole fractions are then obtained by solving the set of coupled n equations provided by Eq. (11). We employ a fixed point iteration approach, where the permeate mole fractions at iteration $s + 1$ are evaluated using the permeate mole fractions at iteration s.

$$\frac{x_i^{p,s+1}}{x_i^r} = \frac{\mu_i^p(T,P_p,\{x_k^{p,s}\}) - \mu_i^r(T,P_r,\{x_k^{r,s}\})}{\sum_{j=1}^n x_j^r \left(\frac{MW_i}{MW_j}\right)^b \left(\mu_i^p(T,P_p,\{x_k^{p,s}\}) - \mu_i^r(T,P_r,\{x_k^{r,s}\})\right)} \tag{12}$$

Where P_p is the permeate pressure, P_r is the retentate pressure, $x_k^{p,s}$ is the permeate mole fraction of species k at iteration s, and $\{x_k^{p,s}\}$ represents the set of all permeate mole fractions at iteration s. Hence, at each iteration the permeate chemical potentials must be updated.

Values of b were adjusted to separation data of a light shale crude measured Sterlitech HP4750X dead-end cell. The model is applied to separation data using membranes $C_6N_6C_6$ and $F_5N_6F_5$. The

retentate pressure was set to 43 bar and the permeate pressure was atmospheric. The temperature was held constant at 50 °C.

Table S8 list the regressed values of b and figure 1 compares model fit to measured SIMDIST. The characterization parameter b for $C_6N_6C_6$ ($b = 1.8$) is less than $F_{13}N_6F_{13}$ ($b = 2.5$) suggesting $F_{13}N_6F_{13}$ is more effective at rejecting heavier species. This can be observed in Fig. 4E which compares experimentally measured SIMDIST of petroleum feed and permeate for each case.

Table S8. Characterization parameter b for separation of light shale crude

Membrane	b
$C_6N_6C_6$	1.8
$F_{13}N_6F_{13}$	2.5

Overall, the 1 parameter model gives a good fit of the separation data. The error in the model predicted SIMDIST at low boiling points (T < 110 °C) may be due to lost light species in the experimental measurement process.

Movie S1. Free-standing nanofilm formation at aqueous-organic interface using concentrated $F_5N_6F_5$ MOA solution (0.2 wt.%) and TMC (0.1 wt.%) reacted for 7 min, followed by transferring the nanofilm onto air-water surface. Obvious shrinkage of nanofilm on the water surface was found. Wrinkles were observed on nanofilm surfaces. The white circle is the original nanofilm disc size at the aqueous-organic interface.